Activity quantification of 177Lu using a 360◦ CZT gamma camera - comparison with a dual-head Anger camera

Albin Lindvall

Supervisors

Anna Stenvall, Johan Gustafsson, and Erik Larsson

Abstract

Background and Aim: New SPECT cameras that use CZT detectors in a 360° configuration has recently been introduced. Together with Bayesian reconstruction methods employing Median Root Prior (MRP) and Relative Difference Prior (RDP), this constitutes an alternative to Anger-based SPECT for activity quantification. The aim of this thesis is to, by the use of both OS-EM and Bayesian reconstruction methods, assess the feasibility of 360° CZT SPECT (GE Starguide™) for activity quantification of ^{177}Lu, using activity quantification of ^{99m}Tc as a baseline and compare its performance to that of an Anger-based SPECT camera (GE Discovery NM/CT 670, 5/8" crystal).

Method: To compare the performance of the cameras for quantitative SPECT, various phantoms in different geometries were imaged in both cameras. First, cylindrical uniform phantoms with ^{177}Lu or ^{99m}Tc were imaged. The images of the uniform phantom with ^{177}Lu was used to optimise the Signal-to-Noise ratios (SNR) of ^{177}Lu energy and scatter windows for 360° CZT SPECT and compare these to Anger-based SPECT. The dependency of the reconstructed signal on position in the Field-Of-View (FOV) of the 360° CZT SPECT was investigated by testing the difference in means of reconstructed signal between Volume-Of-Interests (VOIs) placed in different transaxial and axial positions of the uniform phantoms, for both radionuclides. The dependency of the reconstructed signal on geometry was subsequently investigated by repeated imaging of the same spherical source in different parts of FOV. Then the difference in means of reconstructed signal between the delineated spheres in the different images was tested. Additionally, a point source of ^{177}Lu or ^{99m}Tc was imaged repeatedly by using different source-to-collimator distances. Finally, calibration factors for ^{99m}Tc and both peaks of ^{177}Lu was determined for both systems by relating reconstructed signal to known phantom activity. These calibration factors were then used to compute recovery for spheres, as function of volume in a NEMA body phantom.

Results: The results show that the reconstructed signal of the 360° CZT SPECT has a positional dependency for ^{99m}Tc and both peaks of ^{177}Lu in transaxial and axial directions. The optimal energy window of the 360° CZT SPECT for ^{177}Lu, was asymmetric and was centred at 205.3 keV with a ±5.5 % width using scatter compensation with Triple-Energy-Window(TEW). This energy session was found to achieve improved SNR compared to the Anger-based SPECT for the same acquisition time and activity. The calibration factor of this energy session, regardless of reconstruction method, was found to be 80.2 $\mathrm{s}^{-1}\,\mathrm{MBq}^{-1}$ but had a significant positional dependency (p = 1×10^{-4}) with a 18 % difference at most between the calibration factors found when placing the VOI used for calibration factor determination in different transaxial positions of the uniform phantom. The same energy session used for imaging of a sphere at different FOV positions was similarly found to result in a significant variation in reconstructed signal (p = 2×10^{-17}) with a 9 % difference at most. The point source acquisitions with a varying source-to-collimator distance showed that there was a slight difference in reconstructed signal with different FOV sizes. The recovery of ^{177}Lu and ^{99m}Tc in spheres with different volumes for Anger-based SPECT followed expected trends while the recovery for 360° CZT SPECT displayed unreasonably high recovery for spheres positioned in the upper part of FOV.

Conclusion: The reconstructed signal of 360° CZT SPECT does display a dependency on geometry which makes its use for activity quantification inaccurate. The same dependency is not seen for Anger-based SPECT, which displayed stable calibration factors thus allowing activity quantification with increased accuracy. The 360° CZT SPECT does however, compared to Anger-based SPECT, exhibit an increased SNR as well as a higher recovery, although unstable. Therefore, it displays promising results, should the reason for the unstability be discovered and solved.

Populärvetenskaplig sammanfattning

Radionuklidterapi är en nuklearmedicinsk behandling där man använder sig av ett radioaktivt läkemedel för behandling av diverse sjukdomar, ofta kan det vara olika former av spridd cancer. Det görs genom att administrera radioaktiviteten i patienten där den söker sig till cancern och där strålar och därmed behandlar tumören. Den utsända strålningen från radionukliden består av laddade partiklar vilka absorberas lokalt och därmed behandlar tumören. Men radionuklider kan också sända ut gammastrålning vilken lämnar kroppen och tillåter bildtagning. Lutetium-177 är ett exempel på en radionuklid som används för radionuklidterapi och sänder ut gammastrålning. Målsökningen till cancertumören görs genom att man märker radionukliden till ett kemiskt signalämne som söker sig till så kallade receptorer som cancercellerna uttrycker. I samband med en behandling är det önskvärt att ta bilder av fördelningen av radioaktivitet för att kunna beräkna den absorberade dos av joniserande strålning som patientens friska organ och tumörer har utsatts för. För att beräkna den absorberade dosen måste man först bestämma fördelning och mängd av radioaktivitet i patienten. Detta kallas aktivitetskvantifiering. Det görs genom att använda sig av en gammakamera vilken tar bilder av den kvarvarande radioaktiviteten som tillåter att man beräknar mängden aktivitet i den volym man tar bild av. Traditionellt sett görs detta med en så kallad tvåhövdad Angerkamera vilken använder två kamerahuvuden med strålningsdetektorer vilka roterar runt patienten. De tar då en serie tvådimensionella bilder som tillsammans möjliggör beräkning av en tredimensionell bild av radioaktiviteten.

På senare tid har nya kameratekniker etablerats vilka istället använder sig av flera detektorer i en cirkulär konfiguration runt patienten. Dessa detektorer skiljer sig också från Angerkameran på så sätt att de använder sig av en annan detektionsteknik där strålningen omvandlas till mätbar ström direkt. Angerkameran går istället via ett mellansteg där strålningen först omvandlas till ljus innan den omvandlas till ström. Teoretiskt sett ska den nya kameran tillåta noggrannare aktivitetskvantifiering av Lutetium-177 tack vare en bättre rumsupplösning, energiupplösning och känslighet.

I detta arbete undersöks den nya kamerans lämplighet för aktivitetskvantifiering av Lutetium-177 genom att jämföra den med en Angerkamera. Det görs genom att använda sig av olika så kallade fantom, typiskt plastbehållare i olika geometrier, fyllda med Lutetium-177 vilka placeras i kamerorna och avbildas.

Resultatet av detta arbete visar på att det finns ett oönskat positionsberoende i den nya kamerans bildfält, upp till 18 %. Samma radioaktiva källa ger inte samma signal oavsett var den är placerad i kameran. Det innebär att det blir en osäkerhet när man använder kameran för aktivitetskvantifiering. Uppenbarligen vill man kunna vara så säker som möjligt när man använder en kamera för att beräkna stråldosen till en patient vid en behandling och därför är detta negativt. Samma positionsberoende finns inte i den gamla kameran och även om det krävs längre mättider på den så är den säkrare i nuläget. Men då tillverkaren har gjorts medvetna om det oönskade positionsberoendet är det inte omöjligt att en mjukvaruppdatering lanseras i framtiden som löser problemen.

Abbreviations

- ANOVA - Analysis Of Variance

- BSREM - Block Sequential Regularised Expectation Maximisation

- CZT - Cadmium Zinc Telluride

- DEW - Dual Energy Window

- DOTA - Dodecane Tetraacetic Acid

- FOV - Field Of View

- FWHM - Full Width Half Maximum

- LEHR - Low Energy High Resolution

- MAP - Maximum A Posteriori

- MEGP - Medium Energy General Purpose

- MRP - Median Root Prior

- NEMA - National Electrical Manufacturers Association

- NET - Neuroendocrine tumour

- OS-EM - Ordered Subset-Expectation Maximisation

- OSL - One Step Late

- PMT - Photomultiplier Tube

- PRRT - Peptide Receptor Radionuclide Therapy

- PSMA - Prostate Specific Membrane Antigen

- RC - Recovery Coefficient

- RDP - Relative Difference Prior

- SPECT - Single Photon Emission Computed Tomography

- SSRT - Somatostatin Receptor Targeting Ligands

- TEW - Triple Energy Window

- VOI - Volume Of Interest

Contents

1 Introduction

Ever since the rise of radionuclide therapies in the quest for treatment of illnesses such as hyperthyroidism and cancer, the calculation of absorbed doses to the patients' targets as well as the organs at risk has been desirable. Using this information the patients' treatment can be further individualised and the data can be used to improve the treatment for future patients. Recently, the usage of ^{177}Lu-based radionuclide therapies, mostly in the form of ligands binding to the somatostatin receptor, commonly expressed in neuroendocrine tumours (NETs) has gained popularity in the form of a radiopharmeutical, Lutathera® with its proper name [^{177}Lu]Lu-DOTA-TATE [1], approved by the European Medicines Agency (EMA) in 2017 and the U.S. Food and Drug Administration (FDA) in 2018 [2]. Additionally, Pluvicto™, [^{177}Lu]Lu-PSMA-617 was approved by both EMA and FDA in 2022 [3] [4] for the usage in prostate specific membrane antigen(PSMA) radionuclide therapies [5]. A correlation between the absorbed dose to the tumour and the tumour response has been shown [6] which makes it desirable to individualise therapies, by personalised dosimetry. Therefore, to achieve this, an accurate and reliable method to quantify activity is of utmost importance. Of course, perfect accuracy could never be achieved. But for the measurement of activity of therapeutic radionuclides, international guidelines recommend a radionuclide calibrator accuracy of 5 % [7], meaning an activity quantification accuracy of 5 % would be good, given the current recommendations. An accuracy exceeding 15 % would on the contrary exceed the accuracy of a multitude of activity quantification phantom experiments and can therefore be considered unacceptable [6].

Historically, the use of planar gamma camera imaging for activity quantification has been common practice. This method is however inaccurate with regards to activity quantification due to overlapping structures, with errors that range from roughly 5 % to 50 % with the former only achievable in non-clinical situations and in specific geometries [8]. Another problem of the gamma camera is its inability to determine the size along the projected direction of the target or organ imaged. This makes its application for dosimetry difficult as the depth and thus size of the target is an important factor for the absorbed dose of the emitted radiation. The rise of Single Photon Emission Computed Tomography (SPECT/CT) has allowed for increased accuracy and reliability with regards to activity quantification and thus dosimetry of ^{177}Lu-based radiotherapies [9]. Due to the low yield of the two γ-ray energy peaks of ^{177}Lu the usage of conventional dual headed Anger cameras does come with some disadvantages. Low sensitivity, low energy resolution and the limited spatial resolution restricts the accuracy of the system. In turn, the acquisition times are extended which limits the number of patients that can be examined on a camera. Additionally, this increases the risk of patient movement further decreasing the accuracy. Lately, 360° cadmium zinc telluride (CZT) SPECT cameras has been introduced as an alternative to Anger cameras. The different geometry and detector design allows for better sensitivity and energy resolution and may enable activity quantification with higher accuracy and precision.

1.1 Aim

The aim of the study is to investigate the feasibility of activity quantification of ^{177}Lu, using a 360° CZT SPECT camera of the model GE Starguide™. Additionally, its performance for activity quantification of ^{177}Lu will be compared to a conventional dual head Anger camera, a GE Discovery NM/CT 670 with a MEGP collimator. To achieve this, phantoms filled with labelled ^{177}Lu will be imaged on both systems and then anlysed. As the cameras are optimised for imaging of ^{99m}Tc, activity quantification of this radionuclide will be used as a baseline. Furthermore, measurements that test whether the 360° CZT SPECT camera fulfil qualifications for accurate activity quantification of ^{177}Lu will be performed.

2 Theory

2.1 Radionuclides

2.1.1 ^{177}Lu

^{177}Lu is a radionuclide which decays by β^- with a Q-value of 498.3 keV. It emits β^--particles with a mean kinetic energy of 134 keV, internal conversion electrons and Auger electrons resulting in a mean kinetic energy of all electron emissions of 147 keV with a half-life of 6.65 d [10]. These electrons are absorbed locally for therapeutic purposes. Additionally, it emits two γ-photons useful for ^{177}Lu imaging. These have energies of 112.9 keV and 208.4 keV with associated yields of 6.17 % and 10.36 %. Together with its reliable labeling to a complex, usually dodecane tetraacetic acid (DOTA), in turn bonded to biomolecules used in radionuclide therapy, this makes ^{177}Lu suitable for radionuclide therapy as well as quantitative imaging. Additional γ-photon energies of note is 249.7 (0.2 %) and 321.3 keV (0.2 %).

^{177}Lu is used for labeling of various biomolecules for radionuclide therapy. The two most important examples are the somatostatin-receptor and the PSMA targeting ligands [11]. The somatostatin receptor is a protein that is expressed on the surface of cells throughout the body. In particular, it can be expressed by NETs due to their origin of neuroendocrine cells [1]. The receptor, has a natural ligand, somatostatin, which binds to it. For NETs that express the receptor, this enables peptide receptor radionuclide therapy (PRRT) with ^{177}Lu in the form of $\left[^{177}\text{Lu}\right]$Lu-DOTA-SSRT where SSRT stands for somatostatin receptor targeting ligands [11] such as TATE and TOC, short for ocreotate and octreotide.

Prostate-specific membrane antigen (PSMA) is also a receptor that is expressed on the surface of prostate cancer cells [5]. This enables the use of ^{177}Lu for labelling of PSMA peptides which then target the prostate cancer cells and enable radionuclide therapy.

2.1.2 ^{99m}Tc

^{99m}Tc is a radionuclide used for imaging for diagnostic purposes. It is a meta-stable form of ^{99}Tc and has a half-life of 6.01 h [12]. It emits γ-photons of 140.5 keV with a yield of 88.9 %. As such, it is ideal for nuclear imaging and serves as a good baseline for quantitative SPECT [13]. Additionally, these ideal properties of ^{99m}Tc means that ^{99m}Tc historically has been the most widely used radionuclide for SPECT. In turn, this means that most gamma cameras built and being built today are optimised for imaging of ^{99m}Tc.

2.2 The gamma camera and its application in SPECT

SPECT is a nuclear imaging modality which uses the emission of γ-radiation to create tomographic images of the distribution of activity within a patient. By image acquisition at different angles the three-dimensional distribution of activity in the source can be resolved. It utilises a gamma camera which is able to resolve a spatial distribution of activity that emits γ-radiation. As such, the gamma camera must employ some form of collimation which discriminates photons that don't strike the detector head in the direction that the collimator is designed for. A common type of a collimator is the parallel hole collimator with a mode of operation shown in figure 1. Ideally, it attenuates all photons that hit the collimator, thus only allowing photons to pass through that are directed towards the detector in a certain angle range.
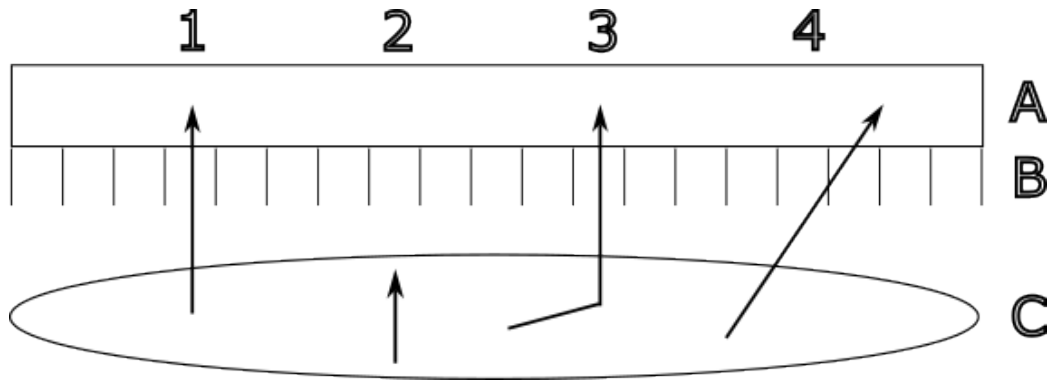
Figure 1: The figure shows the function of a gamma camera with detector (A) equipped with a parallel hole collimator (B). From the representation of a patient (C) four important modes of transport of γ-photons are demonstrated. These are the primary photons that strike the detector perpendicularly from the patient (1), an attenuated photon (2), a scattered photon that strikes the detector that leads to detection in the gamma camera (3) and a photon that penetrated the collimator septa and also gets detected as if it was a primary photon (4).

A parallel hole collimator consists of a map of holes, often in a hexagonal configuration, where the edges of the map, called septa, is made of a material with a high atomic number (Z) and high density to maximise the linear attenuation coefficient and thus maximise the chance of attenuation when the γ-radiation interacts with the septum [14]. There are several types of parallel hole collimators. These can be categorised, firstly, by the γ-ray energy for which the collimator is intended to be used. Secondly, by the resolution and sensitivity of the collimator. The resolution of a collimator, expressed by the collimator's response to a point source, which can be measured by the Full width at half maximum (FWHM) of the line spread function, can be approximated, when omitting contribution from septal penetration, by

$$FWHM \approx d \cdot \frac{D}{T} \tag{1}$$

where d is the width of the collimator hole, D is the distance between the source and the collimator face and T is the thickness of the hole, as seen in figure 2. It follows that the resolution of a gamma camera is far from perfect, which leads to partial volume effects, manifesting itself in the image as spill-over of signal between regions in the image. Similarly, the sensitivity of a collimator for a given thickness of the collimator septa, is proportional to the efficiency at the surface of the collimator

$$Sensitivity \propto d^2/T^2 \tag{2}$$

Using these two categorisations of parallel hole collimators we can define two typical collimators used for ^{99m}Tc imaging and ^{177}Lu imaging. That is the Low-energy High-resolution (LEHR) collimator and the Medium-Energy General-Purpose (MEGP) collimator. Importantly, one may note from equation 2 that the sensitivity of an ideal parallel hole collimator, meaning complete attenuation for photons hitting the septa, does not depend on the source-to-collimator distance. This is a well established fact first discovered by Anger [15].

2.2.1 Image degrading phenomena

There are a number of phenomena that is considered to degrade the attainable quality and the quantitative use of a SPECT image. These are in the order below represented in figure 1, noted by number 2, 3 and 4.

- Attenuation. This is the phenomenon where photons undergo interaction processes that inhibit the path of an emitted photon in the direction of the gamma camera. As such, it is a

meaning the sensitivity is independent of the distance to the collimator. It shall however be noted that this relationship only holds for small source-to-collimator distances. As the distance increases, the solid angle that the collimator face covers, as seen from the emission point of activity, decreases. This results in a smaller chance of the radiation being emitted towards the collimator the larger the distance of the source to collimator. Additionally, the relationship only holds for situations where the collimator faces the source. For cameras where the direction angle of the collimator is varied during the scan, the sensitivity will also no longer be invariant of the source-to-collimator distance due to differences in time of the collimator facing a given point in the field of view. As such, it can be seen that the resolution of a collimator is increased as the collimator hole thickness T is increased. However, this in turn decrease the sensitivity. Therefore, there is a relationship between the two and this constitutes the second distinction between collimators.
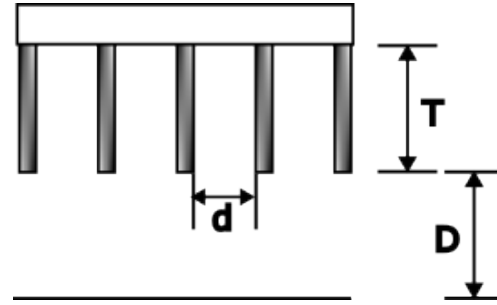
Figure 2: The figure shows distances used for the mathematical description of a collimator hole of parallel hole collimator. T represents the thickness of the collimator, d represents the width of the collimator hole and D represents the source-to-collimator distance.

process that lowers the count rate of a gamma camera. The interaction processes that together make up attenuation are photoelectric effect, Compton scattering, pair production and elastic scattering. As the probability of photon interaction in a beam path increases with the amount of matter that the photon has to travel through, it means that this signal decreasing effect is more apparent in a SPECT image, with an increased size and density of the object imaged as well as the depth of the source within the object. The TF (as in equation 3) of photons in a projection, emitted from position (t′,s′) that is transmitted through matter of varying density and attenuation probability, can be calculated as

$$TF(t', s', \theta) = \exp\left\{ -\int_{s'}^{\infty} \mu(t', s)ds \right\} \tag{3}$$

where $\mu(t', s)$ is the linear attenuation coefficient as function of location along angle θ [16].

- Scatter. This phenomenon is related to attenuation. As the photon interacts with matter the interaction could lead to a change of direction, often via Compton scattering, into a direction against the collimator face that leads to detection in the gamma camera and not attenuation in the septa. This detection contributes to a falsely detected event as the photon appear to be emitted from the position of interaction, not from the true position of emission. Hence, this added contribution to the signal does not reflect the true activity distribution.

- Septal penetration. With a higher γ-ray energy, the linear attenuation coefficient decreases, resulting in an increased probability for a photon to penetrate the collimator septa. Such an event leads to the unwanted detection of a γ-photon which does not reflect the true activity distribution. The contribution from septal penetration is increased with smaller source-to-collimator distance, due to the increased solid angle of the side faces of the collimator septa as seen from the source. [17]. With increased source-to-collimator distance, the effective

thickness of the collimator septum that the photon has to penetrate is increased and thus the probability of septal penetration is decreased.

2.2.2 Anger gamma cameras

The Anger camera is a gamma camera which is based on a scintillation detector that employs Anger logic to determine the position of interaction in the scintillation crystal [18]. The Anger camera consists of a collimator, a scintillation crystal and an array of photomultiplier tubes (PMTs). A scintillation crystal detects ionising radiation by emitting visible light - scintillation light - when the crystal, excited by the ionising radiation, deexcites. By the use of a light guide the visible light is fed to the array of PMTs where the photons interact with a photocathode and thus produce electrons via the photoelectric effect [19]. These electrons are accelerated towards a series of dynodes where the electrons are multiplied and consequentially reaches an anode where an electric current is obtained.

Generally, the scintillation photons from a single interaction event in the scintillation crystal will distribute across a number of PMTs. This distribution of varying signals in the PMTs can be used to determine the position of the interaction in the crystal. This is done by computing the centroid of the outputs of the PMTs, weighted by the respective position of the PMT [20]. The method in a simple form is shown in equation 4 where S_i is the signal in PMT i and (x, y) is spatial coordinates across the plane of the PMT array. Typically, a signal threshold is applied under which the output of a given PMT is discriminated and not included in the computation.

$$\hat{x} = \frac{\sum_{S_i} x_i S_i}{\sum_{S_i} S_i}, \hat{y} = \frac{\sum_{S_i} y_i S_i}{\sum_{S_i} S_i} \tag{4}$$

Anger logic does not allow perfect precision of interaction position due to the finite number of PMTs and the finite number of scintillation photons produced in the crystal leading to statistical fluctuations. The precision can be increased by using PMTs with a smaller entrance face although this increases cost and computation times thus lowering speed. The attainable precision of the determinable interaction position is called the intrinsic resolution [21].

The most common scintillation crystal used in an Anger camera is sodium iodide doped with thallium (NaI(Tl)) as it offers the best trade-off between density and effective Z, scintillation light yield, decay time of the excited electron states and cost [22]. The energy resolution of a single NaI(Tl) scintillation detector is generally considered to be at 7.6 % [23] when detecting 140 keV γ-rays. This value is however raised to about 10 % for an Anger gamma camera using NaI(Tl) due to the finite amount of PMTs and the dispersion of information carriers between these, leading to a worse energy resolution [20].

2.2.3 CZT gamma cameras

A CZT gamma camera is based on pixels of a semiconductor detector based on the crystal cadmium zinc telluride. As a semiconductor detector, it works fundamentally different to the Anger camera. Instead of utilising scintillation light to produce charges, the energy from the ionising radiation is directly converted to charge carriers in the form of electron hole pairs in a semiconductor crystal [24]. Then the number of electron-hole pairs created is proportional to the energy of the energy deposited in the detector. A considerable benefit of semiconductor detectors compared to scintillation detectors is the improved energy resolution. This stems from the increased number of charge carriers per energy unit of deposited energy that the small band gap of semiconductors allows for [22]. The Poisson limiting resolution R is inversely proportional to the square root of the number of charge carriers N as seen in

$$R|_{Poissonlimit} = \frac{2\sqrt{2\ln 2}}{\sqrt{N}} \tag{5}$$

There are other phenomena which determines the resulting energy resolution of a radiation detector but this is the main reason for the improved energy resolution of semiconductor detectors. For CZT this can result in an energy resolution as low as 5.46 % when measuring 140 keV γ-radiation [25] when taking into consideration charge sharing over several anodes.

CZT detectors does however come with a disadvantage compared to Anger gamma cameras. This is related to the collection of the electron hole pairs. When the CZT crystal is subject to an electric field the charge carriers will move towards the electrodes, which induces a current in the circuit. The time-integrated current is then proportional to the deposited energy and registered as an event. The velocity $\vec{v}$ of the charge carriers is given by

$$\vec{v} = \mu \cdot \vec{E} \tag{6}$$

where μ is the carrier mobility and $\vec{E}$ is the electric field [22]. As the charge carriers move within the crystal towards the electrodes they will inevitably encounter crystal impurities. This causes recombination of the charge carriers thus resulting in a lower resulting charge collected. This will in turn mean that the event is registered as a detected event with a lower energy. This phenomenon is called trapping [26] and for a constant electric field across the crystal, the average range λ of the charge carriers is given by

$$\lambda = \mu \cdot \tau \cdot E \tag{7}$$

where τ is the average carrier lifetime and μ and $\vec{E}$ as previously is the carrier mobility and the electric field. It follows that the charge collected from a radiation interaction event with a CZT detector will depend on the position of the interaction within the crystal. Another trait of CZT detectors and their configuration in gamma cameras is charge-sharing where the electron cloud, freed by the energy deposited by the photon interaction, splits between pixel anodes. This causes a split time-integrated current where only the time-integrated current of one of the anodes is detected as an event, which then results in an event with lower energy [27]. Trapping and charge sharing causes together what is known as energy-tailing effects where not all primary photons in a spectrum is registered as full energy photons but some are detected at a lower energy resulting in an energy peak in the spectrum that exhibits a tail. This effect is demonstrated in figure 3 for a CZT spectrum of ^{99m}Tc.
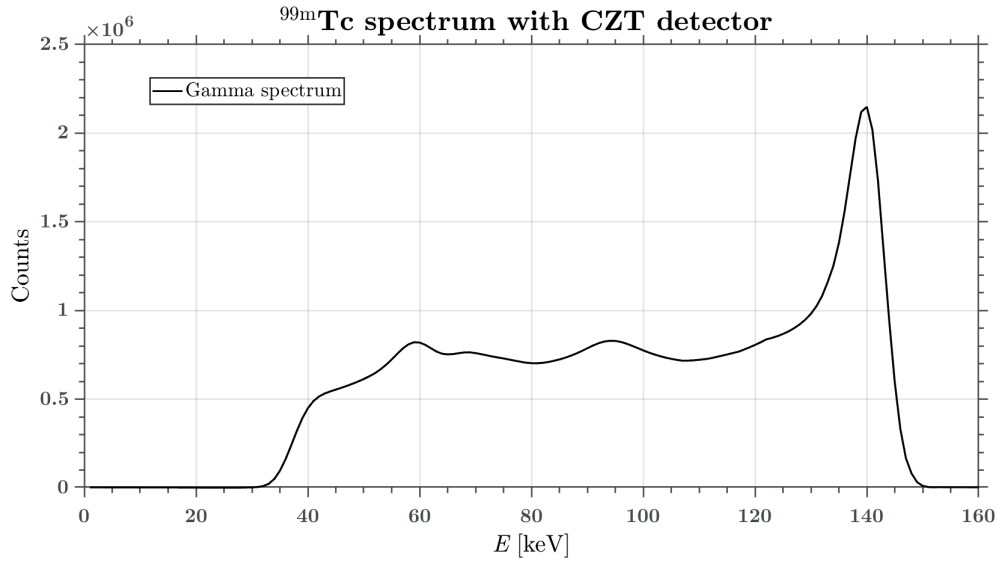
Figure 3: The figure shows a ^{99m}Tc spectrum with a 360° CZT gamma camera representing a CZT detector. The spectrum is recorded by imaging of a uniform cylindrical phantom with ^{99m}Tc. Therefore, the spectrum shows a lot of scatter contribution limiting the visibility of the energy-tailing effects.

2.3   Reconstruction of SPECT images

The act of reconstruction of a SPECT image is the act of using the gamma camera's two-dimensional projections of the activity distribution to construct a three-dimensional image. **P** is a vector with pixel values comprised of the events recorded within an energy window, called the photopeak window. This window ideally only contains primary photons. In an idealised situation, the collection of two-dimensional projections by the camera of the activity distribution can be characterised by the Radon transform. Therefore, the key to the reconstruction problem becomes the inverse to a discrete form of the Radon transform, with a well known solution called the filtered back projection [28]. However, this method is not well suited for SPECT imaging, due to the Radon transform being a deterministic model of the projection process meaning implementation of compensation for image degrading phenomena is difficult. Additionally, since the Radon transform strictly is an analytical expression where no consideration is taken of the randomness of γ-ray emission, the level of noise in the resulting images is high. Therefore, although more computationally intensive, iterative reconstruction methods are preferred. The emission tomography reconstruction problem that is to be solved by an iterative reconstruction can be formulated as an estimation problem [29] and briefly states that an activity distribution **F** shall be found given a set of projections **P** and information about the imaging system **A**. As such, the process to produce projections of the activity distribution can be described as a system matrix **A** multiplied by the source distribution **F** to produce the projections **P**.

$$\mathbf{P} = \mathbf{AF} \tag{8}$$

One iterative reconstruction technique for finding an estimate of **F** is called Maximum likelihood expectation maximisation (ML-EM) [30]. It seeks to maximise the log-likelihood of an underlying activity distribution **F**, yielding the measured projections **P**. It can be expressed as

$$l(\mathbf{F}) = \ln(pr(\mathbf{P}|\mathbf{F})) = \sum_{i=0}^{m-1} \left(p_i \ln([\mathbf{AF}]_i) - \ln(p_i!) - [\mathbf{AF}]_i \right) \tag{9}$$

7

where $[\mathbf{AF}]_i$ is an indexed element of the multiplication of the system matrix and the image matrix. Here we seek to find the activity distribution $\mathbf{F}$ that maximises the log-likelihood. Then the iterative algorithm, ML-EM that maximises the log-likelihood function is

$$f_j^{k+1} = \frac{f_j^k}{\sum_{i=0}^{m-1} a_{ij}} \sum_{i=0}^{m-1} a_{ij} \frac{p_i}{\sum_{q=0}^{m-1} a_{iq} f_q^k}. \tag{10}$$

The algorithm works by using an estimate f_j^k to construct projections as if the estimate was imaged in the system used to capture the measured projections p_i. Then the measured projections are compared to the estimated projections by division before the result is backprojected. The result is normalised and multiplied with the old estimate to yield a new estimate thus completing one iteration of the algorithm.

A common way to accelerate the algorithm is the ordered subset expectation maximisation algorithm [31]. It is a modification of ML-EM where the projections are divided into subsets. Then an update of ML-EM in equation 10 is performed for each subset individually thus yielding a new update of the estimate f_j^k for each subset. One iteration is achieved when updates for all subsets of projections has been performed. It has been shown that OS-EM results in an equivalent result as ML-EM [32] but in a fraction of the time. This is because the time of one iteration of OS-EM being comparable to that of one iteration of ML-EM [29]. However, in one iteration of OS-EM as many updates as the number of subsets used, can be performed.

2.3.1 Bayesian iterative reconstruction

An issue with OS-EM is that the results are notoriously noisy for the number of iterations required to achieve full convergence. A proposed solution to this is Bayesian reconstruction utilising priors [33]. The use of a prior is by regularisation of the reconstruction problem by the employment of a presumption about the true activity distribution. Rigorously, Bayesian reconstructions are based on Bayes theorem [34] which, applied to the reconstruction process, expresses the probability for an underlying activity distribution $\mathbf{F}$ given the measured projections $\mathbf{P}$ as

$$pr(\mathbf{F}|\mathbf{P}) = \frac{pr(\mathbf{P}|\mathbf{F}) \cdot pr(\mathbf{F})}{pr(\mathbf{P})} \tag{11}$$

The task of an iterative reconstruction process then becomes to maximise the likelihood of $pr(\mathbf{F}|\mathbf{P})$ a posteriori. This is called the maximum a posterori (MAP) criterion [29]. As $pr(\mathbf{P})$ is a constant, the expression $ln(pr(\mathbf{F}|\mathbf{P}))$ can be maximised by maximising the expression $\ln(pr(\mathbf{p}|\mathbf{F})) + ln(pr(\mathbf{F}))$ such as

$$ln(pr(\mathbf{F}|\mathbf{P})) \simeq \ln(pr(\mathbf{P}|\mathbf{F})) + ln(pr(\mathbf{F})) = \sum_{i=0}^{m-1} p_i \ln([\mathbf{AF}]_i) - \ln(p_i!) - [\mathbf{AF}]_i + ln(pr(\mathbf{F})), \tag{12}$$

where the term $ln(pr(\mathbf{F}))$ can be represented by a prior in the Bayesian framework. It can be utilised in a Block Sequential Regularised Expection Maximisation-algorithm (BSREM) [35] or in One Step Late-algorithm (OSL) [36] as

$$f_j^{k+1} = \frac{f_j^k}{\sum_{i=0}^{m-1} a_{ij} + \beta(\partial R(f_j^k)/\partial f_j^k)} \sum_{i=0}^{m-1} a_{ij} \frac{p_i}{\sum_{q=0}^{m-1} a_{iq} f_q^k}. \tag{13}$$

Here, $R(f_j^k)$ in $\beta(\partial R(f_j^k)/\partial f_j^k)$, will depend on the chosen prior. It is then added to the normalisation of the backprojection $\sum_{i=0}^{m-1} a_{ij}$. We can then introduce the Bayesian weight β with a value

that controls the level of regularisation of the prior $R(f)$. Clearly, for OSL, as β approaches zero the result becomes equivalent to ML-EM.

Examples of Bayesian Priors used for SPECT are the Median Root Prior (MRP) [33] and the Relative Difference Prior (RDP) [37]. MRP penalises local voxel variations in a reconstructed SPECT image that deviate from it's nearby regions median, M_j. It is implemented as

$$R(f) = ((f_j^k - M_j)/M_j). \tag{14}$$

As such it suppresses noise due to noise in a SPECT image typically manifesting itself as local variations in signal while still retaining quantitative accuracy [33]. RDP penalises voxels in a reconstructed SPECT image that deviate from the values of its neighbouring voxels. It is implemented as

$$R(f) = \sum_j \sum_{k \in N} \frac{(f_j - f_k)^2}{(f_j + f_k) + \gamma|f_j - f_k|}, \tag{15}$$

where N_j is the neigbourhood of voxel j. We also introduce the edge preservation constant γ for RDP which is meant to preserve the edges of the true activity distribution. As for MRP, its purpose is to regularise noise while retaining quantitative accuracy [37].

2.3.2 Compensation for image degrading phenomena

As previously mentioned there are several phenomena that negatively impacts a SPECT image, namely that of attenuation, scatter and septal penetration. For quantitative SPECT in particular, these phenomena causes the number of detected counts in the detectors to be dependent on emission position. In addition, due to the design of collimators there is an imperfect spatial resolution, with a FWHM proportional source-to-collimator distance. Therefore, compensation for image degrading phenomena is wanted for quantitative SPECT.

Compensation for attenuation is based on the use of a patient-specific attenuation map [16] that allows the modeling of attenuation in the object imaged. This can be done in various ways but in practice attenuation maps from other modalities, i.e computed tomography (CT), is used. Statistical iterative reconstruction algorithms are well suited for implementation of attenuation compensation by the use of the attenuation maps. Typically, it is implemented in the projection of the image estimate by weighting the counts of each voxel in the projection depending on the probability of the photon to attenuate on its path towards the detector. This is done by looping through the voxels of the image estimate along the projection angle and weighting its value by the transmission fraction as described in equation 3.

Compensation for scatter can be done in different ways. The most widely used method is energy window based. It defines scatter energy windows, estimated to ideally only contain scattered photon. The projections of the photopeak window are then subtracted by or added to the projections of the scatter energy window, scaled by a factor k. However, as the subtraction of the scatter window events from the main energy window events can lead to negative values it is usually favourable to add a scatter contribution to the estimated projections rather than subtract it. An implementation of a scatter compensation method, called dual energy window (DEW) scatter compensation, that adds the scatter window events to the estimated projections can be used as

$$f(x,y) = \sum_{q=0}^{m-1} a_{iq} f_q^k + N_{SC_i} = \sum_{q=0}^{m-1} a_{iq} f_q^k + \frac{N_{SCW}}{W_{SCW}} W_{main} \cdot k \tag{16}$$

where $\sum_{q=0}^{m-1} a_{iq} f_q^k$ is the projections as seen in equation 10 and 13, N_{SC_i} is the estimated scatter contribution in the photopeak window, N_{SCW} is the signal in the scatter window and W are window

widths [38]. The choice of the scaling factor *k* is not simple as it depends on the imaging system and geometry used. But it is typically set to a value of 0.5 when the energy window and scatter window is the same size [39]. A similar scatter compensation-method is the Triple Energy window (TEW) [40]. It is well suited for imaging of a radionuclide with high energy photon emissions that can undergo down scattering into the photopeak energy window, such as ^{177}Lu. It works by defining two scatter windows, one above the photopeak window in addition to the previous scatter window below the photopeak window. Then the projections of the photopeak window are added by an estimation of the scatter contribution using both scatter windows. It shall be noted that DEW can be viewed as a special case of TEW, for when the scatter window above the photopeak window has a width of zero. Scatter compensation can also be done by modeling the contribution from scatter in the photopeak window by Monte Carlo Simulation [41].

The process of compensating for the imperfect spatial resolution of SPECT and septal penetration can be described as the task of compensating for the collimator-detector response (CDR) of a SPECT system, by modeling of the point spread function of the collimator response. It describes the response of the imaging system to a point source of activity. It can be shown that the shape of the CDR is the primary factor in determining the image resolution of a SPECT system [42] and as such, compensation for the imperfect spatial resolution becomes the task of compensating for the CDR. Its function, the CDRF can be decomposed into several components, one being the intrinsic response of the imaging system characterising the uncertainty in position estimation of the detector system, one being the geometrical component due to the resolution being dependent on the distance from the detector as seen in equation 1 and another being the septal penetration component, also dependent on the distance from the detector. Compensation for the components of the CDR can then be done by plane-wise convolution of the estimated projections from the source distribution, with the CDRF as function of voxel-detector distance.

2.4   360 ° CZT SPECT systems

Recently, whole-body CZT SPECT cameras with a 360° detector configuration has been introduced on the market [43][25]. An example of such a system is Starguide™ by General Electric Healthcare, introduced in 2021.

It has 12 columns of CZT pixelated detector, using a LEHR parallel hole tungsten collimator in a square grid, configured in a ring around the FOV. Each detector column consists of 7 CZT modules, each with 16×16 elements, providing an axial view of 28 cm. Each individual CZT element has a square face of $2.46 \times 2.46\,mm^2$ with a crystal thickness of 7 mm allowing the detection of the high energy γ-photons that ^{177}Lu emits. For attenuation compensation the system is equipped with a CT gantry.

The system design allows individual movement of each detector column allowing close positioning to the activity source, thus improving spatial resolution. During acquisition, each individual detector module swivels across the FOV, thus allowing acquisition of the entire FOV while retaining the close positioning. To enable acquisition from the full solid angle the gantry rotates after each full swivel motion. The swiveling motion can be performed in two modes, either continuous where the data is binned into discrete projections or step and shoot mode where the projections are made separately. Additionally, the swiveling motion of the detectors allows a focus mode where a transaxial area of the FOV is defined as a focus, resulting in a focused VOI. Then the detectors will focus on this area for a set amount of relative time, 51 % to 100 %. This increases the angular sampling and thus increases the acquisition time for this VOI, on the cost of lower acquisition time for the remaining parts of the FOV [43]. A demonstration of the swiveling motion over a focused FOV is presented in figure 4.

These traits of the GE Starguide™ makes it theoretically well suited for ^{177}Lu imaging and ac-

The sensitivity of similar systems are reported to be higher than for Anger Cameras leading to reduced acquisition times by a factor of 2 or 3 [25]. This is mainly because of the simultaneous 360° acquisition. The thinner thickness of the CZT crystal (7 mm) compared to a typical NaI(Tl) scintillation crystal (9 mm) is offset by the high effective Z and density of CZT, leading to a high linear attenuation coefficient compared to NaI(Tl) scintillation crystals [22].

The energy resolution of the system at 208 keV and 113 keV has been measured by Ferri et. al. and is reported to be, as expressed by the FWHM of the photopeaks, 4.9(2) % and 7.7(3) %, respectively [44].
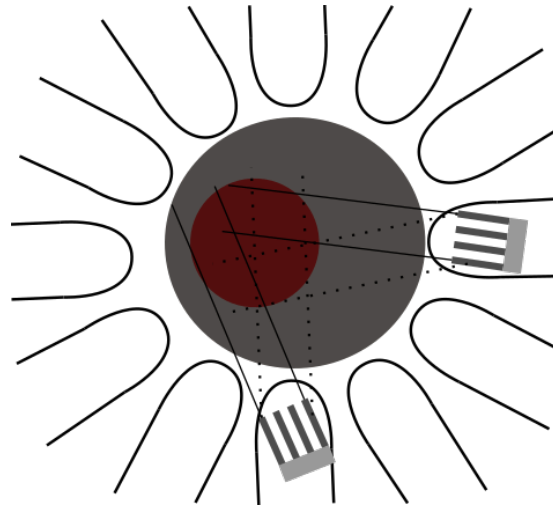
Figure 4: The figure shows a demonstration of the swiveling motion of two of the detectors of the GE Starguide™. The gray area represents the full FOV and the red area represents a focused area. The lines represent detector angles.

tivity quantification of the nuclide. The high sensitivity of the system allows for short acquisition times despite the low yield of the radionuclide. The high energy resolution allows for acquisition of both the 208-peak and the 113-peak with the LEHR collimator. It shall be noted that the use of the LEHR collimator means that the photopeak window of the 208-peak is subject to a substantial amount of septal penetration. The software does allow compensation for this. In return, the LEHR collimator retains the high resolution of such a collimator compared to a MEGP collimator which is typically used for imaging of ^{177}Lu when using an Anger camera. Combined with the close projection distances to the patient this results in ^{177}Lu images with high spatial resolution. Indeed, simulations by Huh et. al of a similar system has been made where a 9.5 mm rod with ^{177}Lu was resolved using a 3 min acquisition time [45]. The same study reached an image contrast of 57 % for ^{177}Lu with a 6 min acquisition time. Additionally, Song et. al concluded that qualitative SPECT imaging with GE Starguide™ at 2 h or 4 h after administration of ^{177}Lu based radionuclide therapies, using an acquisition time of 3 min per bed-position was feasible [46].

3 Materials and methods

3.1 Gamma cameras and reconstruction tools

This project was conducted on a GE Discovery NM/CT 670 (GE Healthcare, Haifa, Israel), with a 5/8" crystal and a GE Starguide™ (GE Healthcare, Haifa, Israel) where the former represented a two-headed conventional Anger-based SPECT camera and the latter represented a 360° CZT SPECT camera.

For imaging of ^{99m}Tc with Anger SPECT a low energy high resolution collimator (LEHR) was used while a medium energy general purpose collimator (MEGP) was used for imaging of ^{177}Lu. All measurements on the Anger SPECT was reconstructed using Hybrid Recon version 4.0 by Hermes Medical Solutions. For ^{177}Lu, this program allowed reconstructions using the 208-peak or both peaks. It did not allow reconstructions using only the 113-peak. Acquisitions on Anger SPECT with ^{99m}Tc was made using a ±10 % energy window, the 113-peak of ^{177}Lu was also made using a ±10 % energy window and the 208-peak of ^{177}Lu was made using a ±7.5 % energy window. All reconstructions with the system, unless noted, were made using compensation for attenuation - using

CT for acquisition of a linear attenuation map - and scatter as well as resolution recovery. The compensation for scatter was based on Monte Carlo simulated data. The program used the one step late (OSL) algorithm to implement the MRP and RDP priors for Bayesian reconstructions.

The reconstructions of the measurements using $360°$ CZT SPECT were done using GE Healthcare's own program Smartconsole, version 1.6.0. Smartconsole allows for modifications of acquisitions made in list mode, where the raw data from a measurement can be manipulated and divided into an optional number of realisations thus simulating shorter scans. Smartconsole allows reconstruction by OS-EM as well as a Block Sequential Regularised Expectation Maximisation (BSREM)-algorithm, which can incorporate the Bayesian priors MRP and RDP. Aside from resolution recovery, attenuation compensation - using CT for acquisition of linear attenuation map - and window based scatter compensation the program also allows penetration compensation for 208 keV. The program does not offer reconstruction without resolution recovery.

All analysis and figures to present results was done in MATLAB2023a using add-ons Image Processing Toolbox, Curve Fitting Toolbox, Statistics and Machine Learning Toolbox assisted by Professional Plots [47] for figure creations.

3.2 Choice of energy sessions for reconstruction of ^{177}Lu images on $360°$ CZT SPECT

To begin with, energy sessions are defined in this work as a set of energy windows comprised of a main energy window, for collection of primary photons combined with one or two scatter energy windows for collection of scatter used for scatter compensation with either DEW or TEW.

For the 208.4 keV energy peak, henceforth simply referred to as the 208-peak, two main energy windows were chosen. The width of the first window was taken to be the twice the width of the FWHM of the photopeak at this energy, previously found to be 4.9(2) %. To increase statistics, a ± 5.0 % energy window width was chosen, centred at the photopeak. Secondly, an assymetric window was chosen, used for ^{177}Lu quantification with a CZT-based gamma camera by Roth [26], to account for the energy-tailing effects of CZT detectors. This energy window was centred at 205.3 keV keV with a width of ± 5.5 %.

For the energy peak at 112.9 keV, referred to as the 113-peak, energy sessions based on two main energy windows were selected. The first window's width were taken to be twice the width of the FWHM of the photopeak at this energy, previously found to be 7.7(2) %. To increase statistics, a ± 7.9 % energy window width was chosen, centred at the photopeak. The second main energy window for the energy peak at the 113-peak was selected to be assymetric according to Roth [26]. This energy window was centred at 110.6 keV with a width of ± 7.5 %.

Subsequently, scatter windows for the selected main energy windows were chosen. For the 208-peak both scatter windows employing the DEW and TEW scatter compensation methods were selected. Only the TEW scatter compensation method was used for the 113-peak. The positions of the scatter windows were selected to be adjacent to the main energy window. Furthermore, the choice of scatter window widths as suggested by Ito et. al [48] were used.

For imaging of ^{99m}Tc the default energy session, provided by the system was used. All energy sessions and energy windows evaluated and later used in this thesis are presented in tables 1 and 2.

Table 1: Energy sessions, comprised of energy windows combined with scatter windows, used for evaluation. Also presented is the energy session used for [99mTc] imaging throughout the work. The positions of the scatter windows are selected to be adjacent to the main energy window.

Name	Energy Peak [keV]	Energy window center [keV]	Energy window width ±[%]	Low scatter window width ±[%]	High scatter window width ±[%]
SG.Lu208A	208	208.4	5.0	3.0	2.0
SG.Lu208B	208	208.4	5.0	4.0	N/A
SG.Lu208C	208	205.3	5.5	2.1	1.7
SG.Lu113A	113	112.9	7.9	4.0	3.0
SG.Lu113B	113	110.6	9.0	2.1	1.6
SG.Tc	140	140.5	10	5.0	N/A

Table 2: Energy windows used for Anger SPECT. No scatter windows are presented as monte-carlo based scatter compensation was used for the reconstruction of the measurements of this camera.

Name	Energy Peak [keV]	Energy window center [keV]	Energy window width ±[%]
Ang.Lu208	208	208.4	7.5
Ang.Lu113	113	112.9	10
Ang.Tc	140	140.5	10

13

3.3 Phantoms

5 different phantom geometries were used. All activities were measured using a Capintec CRC-55tR that had been calibrated for respective radionuclide and geometry.

3.3.1 Uniform Jaszczak Phantom

The Jaszczak cylindrical phantom, without any inserts, was used and had a nominal volume of 6800 ml according to [49].

3.3.2 NEMA Body Phantom

The NEMA Body Phantom was used with 6 spheres with inner diameter 10 mm, 13 mm, 17 mm, 22 mm, 28 mm and 37 mm[50]. The hot spheres were placed in a cold background compartment of water.

3.3.3 Single large sphere

This phantom was a single, large sphere with an inner diameter of 60 mm [51]. The hot sphere was placed in a cold background compartment of water, in the Jaszczak phantom.

3.3.4 Single sphere in different geometries

The fourth geometry used was once again a single sphere attached to a Jaszczak phantom. This sphere had an inner diameter of 31 mm [52]. The sphere was measured with air and water in the background compartment. By rotating the phantom and re-screwing the rod with the sphere to the phantom, five different positions in the FOV were achieved.

3.3.5 Point source

The final phantom used was simply activity in a syringe that was supposed to emulate a point source.

3.4 Camera measurements

The phantoms above were imaged in the Anger SPECT and the 360° CZT SPECT, using continuous sweeping mode of the detectors.

3.4.1 Jaszczak

The uniform Jaszczak phantom was separately filled with ^{99m}Tc or ^{177}Lu and imaged in the Anger SPECT and the 360° CZT SPECT. The activity, activity concentration and acquisition times are presented in table 3.

3.4.2 NEMA

The spheres of the NEMA phantom was separately filled with ^{99m}Tc or ^{177}Lu and imaged in the Anger SPECT and the 360° CZT SPECT. The activity, activity concentration and acquisition times are presented in table 3.

Additionally, the single large sphere, was filled with ^{177}Lu from the same batch used to fill the NEMA phantom and was also imaged with the same protocol. The activity, activity concentration and acquisition times are presented in table 3.

3.4.3 Single sphere in different positions of FOV

The single sphere in different positions was separately filled with ^{99m}Tc or ^{177}Lu and imaged only in the 360° CZT SPECT. A series of measurements were made where the position of the sphere was varied.

Measurements were made both with the background compartment of the phantom empty and filled with water. The variations in the spheres' position are shown in figure 9. The five different positions were chosen to cover the field of view as extensively as possible. The positions will henceforth be referred to their anatomical positions, anterior, sinister, central, dexter and posterior, for a fictitious patient lying supine, head first in the camera. Figure 10 shows the two screw threads that the spheres', connected to a rod, was fixated to. Position anterior, sinister, dexter and posterior were achieved by attaching the sphere to the same screw thread and rotating the phantom. Position central did not utilise the centre screw thread of the Jaszczak phantom because it was broken and the closest available screw thread was used instead. The activities of the spheres (numbered 7 and 8 in table 3) were chosen to be relatively high, to achieve a high count rate and thus a high amount of data to limit noise. The ratio between the activities of the two isotopes was chosen to achieve comparable count rates across the various experiments.

The measurements, aside from being separated into sets with different isotopes were also divided into sets with and without the Jaszczak phantom filled with water. This was done to investigate the effects of attenuation and scatter, and to assess the corresponding reconstruction compensation. A total of 20 measurements were made with an acquisition time of 10 minutes. Care was taken to ensure that the sphere positions across all sets of measurements were consistent. However, axial positions were not considered and hence an assortment of different axial positions were used. The activity, activity concentration and acquisition times are presented in table 3, as phantom name Position.

3.4.4 Point source acquisitions with different FOV sizes

The point source with ^{99m}Tc and the point source with ^{177}Lu was imaged in 360° CZT SPECT. For each source, four separate measurements were made with varying image field sizes, ranging from smallest possible size to a large field size which was assured to be larger than what would be required for a typical patient. The different areas scanned is shown in figure 11. For both radionuclides the same scan areas was used and are referred to as smallest, small, large and largest in order of increasing size. In all measurements the source was placed in the centre of the scan area, as close to the centre of the FOV as possible. The activity and acquisition times are presented in table 3, as phantom name Distance.

Table 3: The table displays the activities and corresponding activity concentrations utilised in the various measurements conducted as part of the project. The activities represent the activity used at the time of acquisition of the first camera system used. The acquisition times represent the true physical durations of acquisition. These were adjusted in the analysis to yield fictitious equal acquisition times between cameras.

Phantom	Radio-nuclide	Activity [MBq]	Activity Concentration [MBq/ml]	Acquisition time [min] 360° CZT SPECT	Acquisition time [min] Anger SPECT
Jaszczak	^{99m}Tc	234	0.034	60	40
NEMA	^{99m}Tc	14	0.27	25	40
Jaszczak	^{177}Lu	384	0.057	60	45
NEMA	^{177}Lu	432	1.8	60	45
Position	^{99m}Tc	41	2.5	10	N/A
Position	^{177}Lu	189	10	10	N/A
Distance	^{99m}Tc	75	N/A	5	N/A
Distance	^{177}Lu	480	N/A	15	N/A

3.5 Evaluation and optimisation of energy sessions for ^{177}Lu imaging with 360° CZT SPECT

To evaluate the different energy sessions, images of the uniform Jaszczak phantom, filled with ^{177}Lu were used. They were reconstructed with 15 iterations and 10 subsets of OS-EM, using resolution recovery and compensation for attenuation, scatter as well as penetration for energy sessions using the 208-peak. These were analysed using two methods. Firstly, the total signal within a VOI placed in the center of the phantom was measured. The VOI, shown in Figure 5, ranged over 10 centrally placed slices. Secondly, the SNR within the same VOI was computed using Equation 17. The SNR and signal within the VOI were then plotted, and the results were used to guide the choice of energy sessions for future measurements.

$$SNR = \frac{\bar{S}}{\sigma_S} \tag{17}$$

Here, $\bar{S}$ denotes the average intensity of pixel values within the VOI and σ_S is the voxel-to-voxel standard deviation within the VOI.

3.6 Evaluation of prior weights for RDP and MRP

In order to compare images from Anger SPECT with those from 360° CZT SPECT using Bayesian reconstruction techniques that employ MRP and RDP it was necessary to determine equivalent values of the Bayesian weight β for MRP and Bayesian weight β and the edge preservation constant γ for RDP. Equivalent values of β and γ between the two cameras was defined as those that produced an equal influence on SNR in a uniform phantom.

To achieve this, images of the uniform Jaszczak phantom, filled with ^{99m}Tc, were evaluated by making a set of Bayesian reconstructions with energy session SG.Tc, using MRP and RDP. For MRP one set was made for each camera where the Bayesian weight β was varied. For RDP two sets were made for each camera. First a set where γ was fixed to unity and β varied and then a set where β was fixed to 0.01 for 360° CZT SPECT and fixed to 0.05 for Anger SPECT and the edge preservation constant γ was varied.

Images were analysed by the measurement and comparison of SNR. SNR was measured by placing a cylindrical VOI, as shown in figure 5 in the central 10 SPECT slices of the phantom. The

360° **CZT SPECT**

Anger SPECT
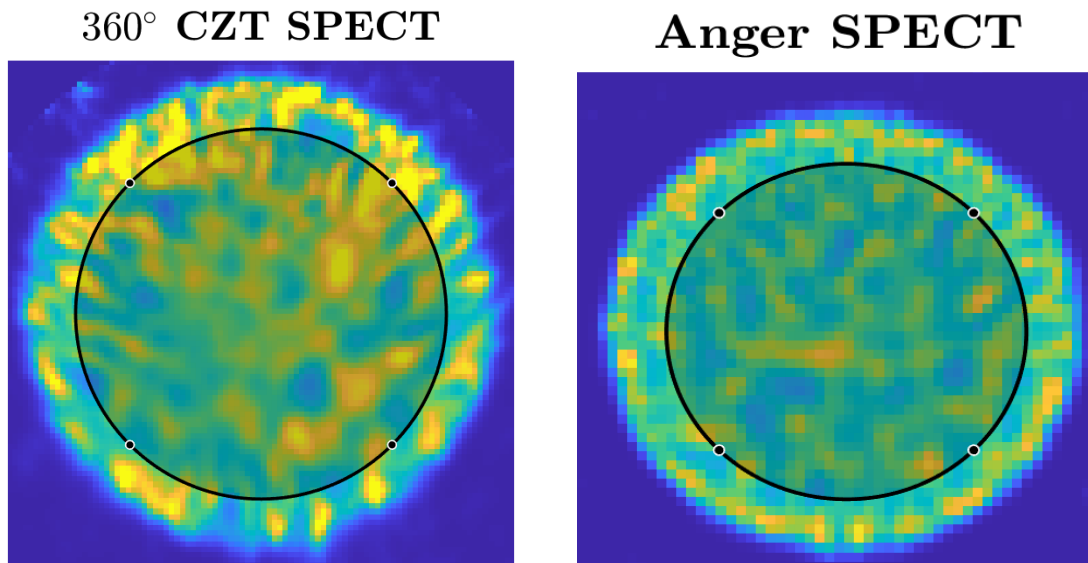
Figure 5: The figure illustrates the placement of the VOI, which was used for various analyses of the 360° CZT SPECT during the project. The VOI was selected to be in the center of the phantom and consists of 10 centrally placed slices. The image used to demonstrate the VOI was reconstructed using energy session SG.Lu208C and OS-EM with 15 iterations and 10 subsets. The phantom used in the image was filled with 384 MBq ^{177}Lu and was of the Jaszczak type.

Figure 6: The figure illustrates the placement of the VOI, which was used for various analyses of the Anger SPECT during the project. The VOI was selected to be in the centre of the phantom and consists of 10 centrally placed slices. The image used to demonstrate the VOI was reconstructed using a 10 % window centred at the 208-peak and reconstructed with OS-EM using 15 iterations and 10 subsets. The phantom used in the image was filled with 384 MBq ^{177}Lu and was of the Jaszczak type.

SNR was calculated by the use of equation 17. For the sets where β was varied, all values of SNR were normalised against the SNR of the image were β was set to zero - that is, where the prior had no effect on the reconstruction. For the set where γ was varied, the SNR values were instead normalised against SNR of the image where γ was set to unity. The resulting normalised SNR values were then plotted against β and γ, with the goal of selecting MRP and RDP parameters for both cameras that would result in an equivalent SNR adjustment and allow comparison between the resulting reconstructed images.
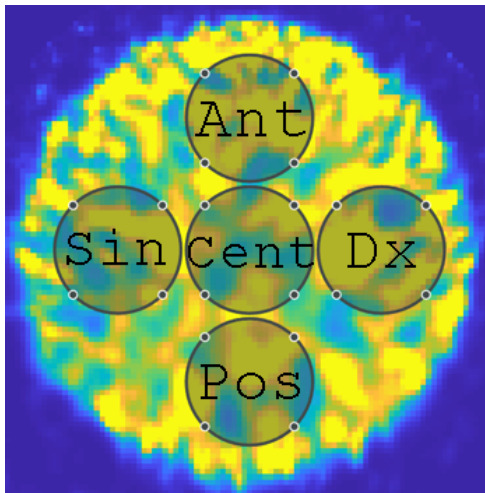
3.7 The dependency of the reconstructed signal on geometry with 360° CZT SPECT

3.7.1 Variations of reconstructed signal with uniform phantom

The dependency of the reconstructed signal on geometry of the 360° CZT SPECT was first investigated by the analysis of the uniform Jaszczak phantom filled with both ^{99m}Tc or ^{177}Lu. The measurements, acquired in list mode, was divided into six separate measurements. Analysis was performed on three images, divided into separate measurements. The images with ^{177}Lu were reconstructed using energy session SG.Lu208C and SG.Lu113B while images with ^{99m}Tc were reconstructed using energy session SG.Tc. All images were reconstructed using OS-EM with 15 iterations and 10 subsets with resolution recovery and compensation for attenuation and scatter. In the case of the image acquired with the 208-peak, compensation for penetration was also applied.

Initially, the dependence of the signal on the position of the VOI transaxially, was analysed by summarising 10 central SPECT slices in the axial direction of the Jaszczak phantom. Then 5 equally sized VOIs was placed in the resulting slice at different positions of the phantom. The posititions of the VOI are shown in figure 7.

Subsequently, the dependence of the signal on VOI position in axial direction was analysed by placing a VOI as shown in figure 5 in five different axial segments, each consisting of ten slices.

Figure 7: The figure shows the placement of the VOIs used to analyse the dependency of the reconstructed signal on geometry using the 360° CZT SPECT image of the Jaszczak phantom in lateral and coronar directions. The image used to demonstrate the VOI placements is the sum of 10 central slices of the phantom with ^{177}Lu. The image is reconstructed using energy session SG.Lu208C and OSEM with 15 iterations and 10 subsets. The different VOIs are named as the anatomical positions of a hypothetical patient lying supine, head first in the camera, that is, anterior, sinister, central, dexter and posterior.
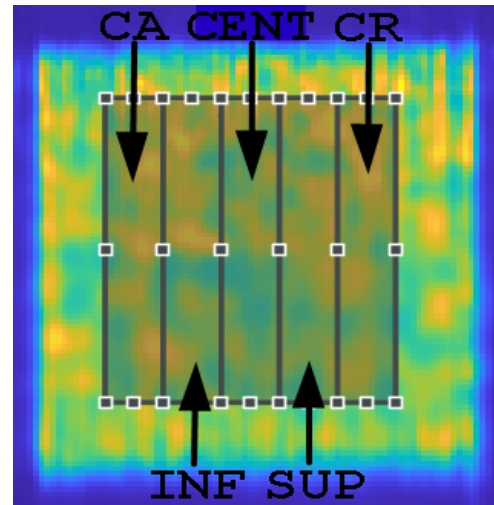
Figure 8: The figure shows the placement of the VOIs used to analyse the dependency of the reconstructed signal on geometry using the 360° CZT SPECT image of the Jaszczak phantom in axial directions. The image used to demonstrate the VOI placements is the sum of 20 lateral slices of the phantom with ^{177}Lu. The image is reconstructed using energy session SG.Lu208C and OSEM with 15 iterations and 10 subsets. The different VOIs are named as the anatomical positions of a hypothetical patient lying supine, head first in the camera, that is, caudal, inferior, central, superior, cranial.

Furthermore, to visualise the signal dependence on position qualitatively, images of the three energy sessions were constructed by summing 20 slices in the axial direction centrally in the Jaszczak phantom. The resulting images were filtered in the spatial domain by convolution with a circular mean filter with a radius of 5 pixels. All pixel values were then normalised against the highest pixel value in the image.

Finally, the dependency of the reconstructed signal on axial position was visualised by summing the total signal in each slice and plotting it against axial slice position.

3.7.2 The delineated reconstructed signal of a sphere as function of position in FOV

The measurements of the singles sphere imaged in different FOV positions were divided into 10 different realisations, each with an fictitious acquisition time of 57 sec. These realisations were made for the ^{177}Lu measurements by using energy session SG.Lu208C and SG.Lu113B, and energy session SG.Tc for the ^{99m}Tc measurements. Subsequently, all 300 realisations were reconstructed using 15 iterations and 10 subsets of OS-EM with resolution recovery and compensation for attenuation and scatter. The realisations using energy session SG.Lu208C additionally used compensation for penetration. Then spherical VOIs with radii as the physical spheres were placed in all images. The centre position of the VOI was based on the sum of all 10 images within the set and was taken as the centre of mass, in a scenario where the voxel signal intensities represent discrete masses, within a spherical VOI with a radius large enough to encapsulate the entire sphere with margin. The centre of this intermediate VOI was determined based on user input.
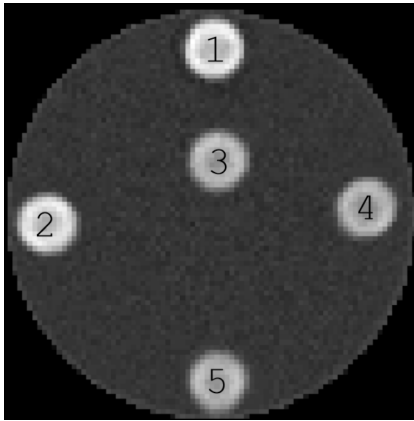
Figure 9: The figure shows the 5 sphere positions in these measurements. The positions are 1 - Anterior, 2 - Sinister, 3 - Central, 4 - Dexter and 5 - Posterior for a ficitious patient lying supine head first in the camera. The image is constructed by manually fusing 5 SPECT slices of the sphere in the different positions to 1 CT-slice from a single measurement. Therefore, the representation is not exact but serves as a demonstration.
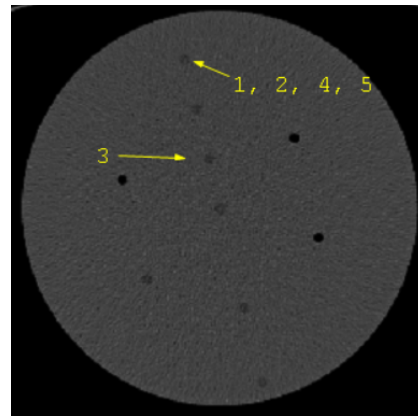
Figure 10: The figure shows the two screw threads that the rod with the activity filled sphere was attached to. To achieve sphere positions 1, 2, 4 and 5 by using the same screw thread, the phantom was rotated. The image shown is a CT-slice from one of the measurements of the screw threads in the Jaszczak phantom.

The total signal in the VOI, taken to be the sum of all voxel values within the VOI was computed and divided by the acquisition time. All signals were corrected for decay. Hence, this yielded 30 sets of signals. Five sets corresponding to the different positions for both peaks of ^{177}Lu with and without water, and five sets of ^{99m}Tc with and without water in the background compartment.

3.7.3 Measurements of point source with varying image field sizes

The ^{99m}Tc image set was obtained using energy session SG.Tc. The reconstructions employed OS-EM with 15 iterations and 10 subsets, as well as BSREM with the RDP prior, with the same number of iterations and subsets. The RDP parameters are shown in table 4. All images underwent attenuation compensation, scatter compensation by the DEW method and resolution recovery.

The ^{177}Lu image set was acquired using energy sessions SG.Lu208C and SG.Lu113B. The same reconstruction method as for ^{99m}Tc was used, with the same parameters. Images reconstructed with the 208-peak were additionally subjected to penetration compensation.

The point source was encapsulated in all images by a spherical VOI with a radius of 5 cm. Then the reconstructed signal within this VOI was normalised against length of acquisition time. This was done for all reconstructions and then plotted as function of FOV size.
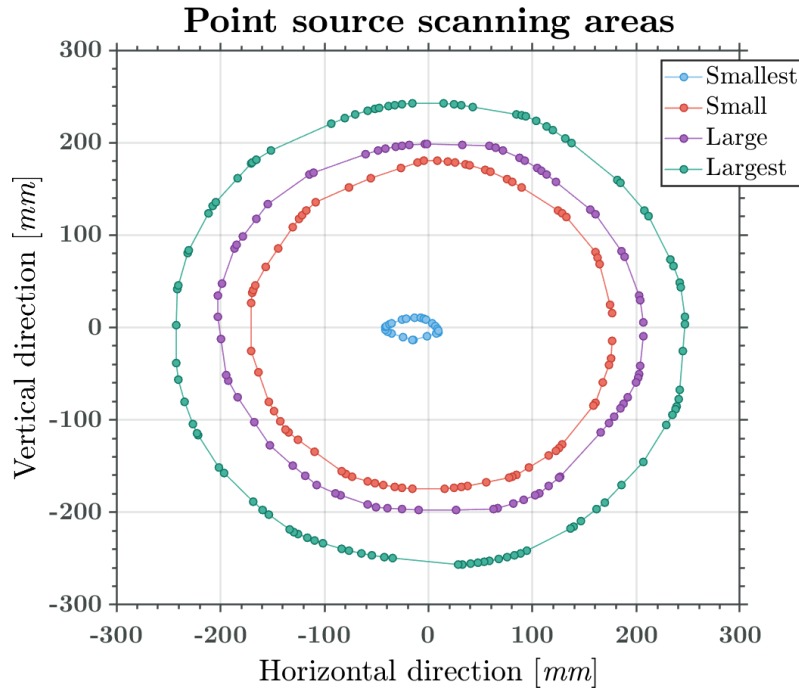
Figure 11: The figure shows the areas scanned during the point source measurements.

3.8 Statistical evaluation

Statistical tests were done for two analyses. Firstly, for the analysis of the dependency of the reconstructed signal on transaxial and axial position when using the uniform Jaszczak phantom. Secondly, it was done for the analysis of the dependency of the reconstructed signal when imaging the single sphere repeatedly in different positions of FOV. One-way ANOVA tests were performed for ^{99m}Tc and both peaks of ^{177}Lu with the null hypothesis that there was no difference in means of the reconstructed signal within the VOIs, shown in figures 7 and 8, as well as no difference in means of the delineated reconstructed signal of the single sphere imaged in different FOV positions, both when placed in a phantom background compartment with and without water.

3.9 Comparison between $360°$ CZT SPECT and Anger SPECT with regards to image quality and activity quantification

The noise levels of the images taken with the two camera systems were analysed by measuring and comparing the SNR of measurements of the uniform Jaszczak phantom, using the same fictitious acquisition times. Such a method does however pose a challenge since the voxel sizes vary between the cameras.

The closest possible voxel sizes for reconstructions with ^{99m}Tc and the 113-peak of ^{177}Lu were 4.92 mm and 4.42 mm, both isotropically for $360°$ CZT SPECT and Anger SPECT respectively. For the 208-peak of ^{177}Lu, measured with $360°$ CZT SPECT and reconstructed with penetration compensation only a voxel size of 2.46 mm was available. Then SNR was evaluated by placing a VOI centrally in a uniform Jaszczak phantom as shown in figure 5 and SNR was calculated by the use of equation 17. Thus, SNR evaluations were made for both ^{99m}Tc and both peaks of ^{177}Lu images using energy sessions SG.Tc, SG.Lu208C and SG.Lu113B respectively. Both OS-EM and Bayesian reconstructed images were evaluated. For the reconstructions using MRP and RDP, to achieve an equal improvement of SNR, equivalent β-values as determined from the method described in sec-

tion 3.6 was used. The chosen values of β are shown in table 4. The edge preservation constant γ as used in reconstructions utilising RDP was always fixed to unity.

Table 4: The table shows the values of the Bayesian weight β used when comparing Anger SPECT and 360° CZT SPECT in terms of SNR and recovery.

Camera	β - MRP	β - RDP
Anger SPECT	0.1	0.08
360° CZT SPECT	0.005	0.003

3.9.1 Determination of calibration factors

Calibration factors were determined from measurements of the uniform Jaszczak phantom filled with ^{99m}Tc and ^{177}Lu. The images were reconstructed using OS-EM with 15 iterations and 10 subsets with resolution recovery and compensation for attenuation, scatter and penetration for the 208-peak. For the ^{177}Lu measurements, reconstructions were made with energy sessions SG.Lu208C and SG.Lu113B, while for the ^{99m}Tc reconstruction was performed with energy session SG.Tc. Reconstructions were also performed with BSREM, using MRP and RDP, to evaluate how the resulting calibration factor would differ compared to the calibration factor of the image with the same energy session and reconstructed with OS-EM. Values of the Bayesian weight β were set to the values shown in table 4.

For Anger SPECT $\pm 10\,\%$ energy windows were used for the 113-peak of ^{177}Lu and ^{99m}Tc while a $\pm 7.5\,\%$ energy window was used for the 208-peak of ^{177}Lu. Reconstructions were made using OS-EM and Bayesian reconstruction, with 15 iterations and 10 subsets and utilising resolution recovery and compensation for attenuation and scatter. The values of the Bayesian weight β are presented in table 4. Calibration factors were computed for all reconstructions by placing VOIs in the 20 central slices of the Jaszczak phantom, as depicted in figure 5 and 6. Equation 18 was then used to compute the calibration factors.

$$k = \frac{N}{A \cdot t} \tag{18}$$

where k is the computed calibration factor, N is the total intensity in the VOI, A is the known activity in the VOI and t is the physical acquisition time.

3.9.2 Assessment of recovery

To evaluate the recovery of the systems, images of the NEMA-phantom were used. For the recovery of ^{177}Lu measurements with the large sphere was additionally included. Furthermore, for reconstructions with OS-EM the average recovery of the single sphere in a water background, positioned in different parts of FOV was included. The reconstruction protocols described in 3.9.1 were used for all measurements. Recovery was then evaluated by using the calibration factor for each reconstruction protocol, as computed by the use of equation 18. The spheres were delineated using spherical VOIs with radii identical to the physical radii of the spheres. The centre of the VOI was determined by computing the centre of mass, in a scenario where the voxel signal intensities represent discrete masses, within a spherical VOI with a radius large enough to to encapsulate the entire sphere. The centre of this intermediate VOI was determined based on user input. The recovery coefficient was then computed using equation 19,

$$RC = \frac{N}{t \cdot k \cdot A} \tag{19}$$

where RC is the recovery, N is the signal within the spherical VOI, t is the acquisition time, k is the calibration factor as determined in section 3.9.1 and A is the known activity of the sphere.

4 Results

4.1 Choice and optimisation of energy sessions for reconstruction of ^{177}Lu images on $360°$ CZT SPECT

Table 5 presents the calculated mean of the signal ($\bar{S}$) as well as the SNRs within a uniform phantom with ^{177}Lu for the energy sessions investigated. The results show that energy session SG.Lu208C (centred at 205.3 keV, $\pm 5.5\%$) exhibits the highest SNR of all energy sessions and also displays the highest signal of the energy sessions of the 208-peak. Energy session SG.Lu113B does display the highest signal out of all energy sessions and the highest SNR of the energy sessions of the 113-peak. However, the SNRs of the energy sessions using the 113-peak is without exception lower than the energy sessions using the 208-peak. The two energy sessions that yielded the highest signal and SNR for both the 208-peak and the 113-peak was energy sessions SG.Lu208C and SG.Lu113B. These are visualised using a ^{177}Lu spectrum from the $360°$ CZT SPECT in figure 12.

Table 5: The table presents the average signals and SNR of the VOIs placed in the uniform phantom, seen in figure 5 with ^{177}Lu using the energy sessions described in table 1. The values are the means of three similar manually placed VOIs and the value within the parenthesis is the standard deviation of these.

Energy session	$\bar{S}$ [a.u]	SNR
SG.Lu208A	225.4(7)	4.28(6)
SG.Lu208B	239.5(9)	4.39(7)
SG.Lu208C	268.8(6)	4.55(5)
SG.Lu113A	278.7(2)	2.33(3)
SG.Lu113B	322.4(3)	2.35(3)
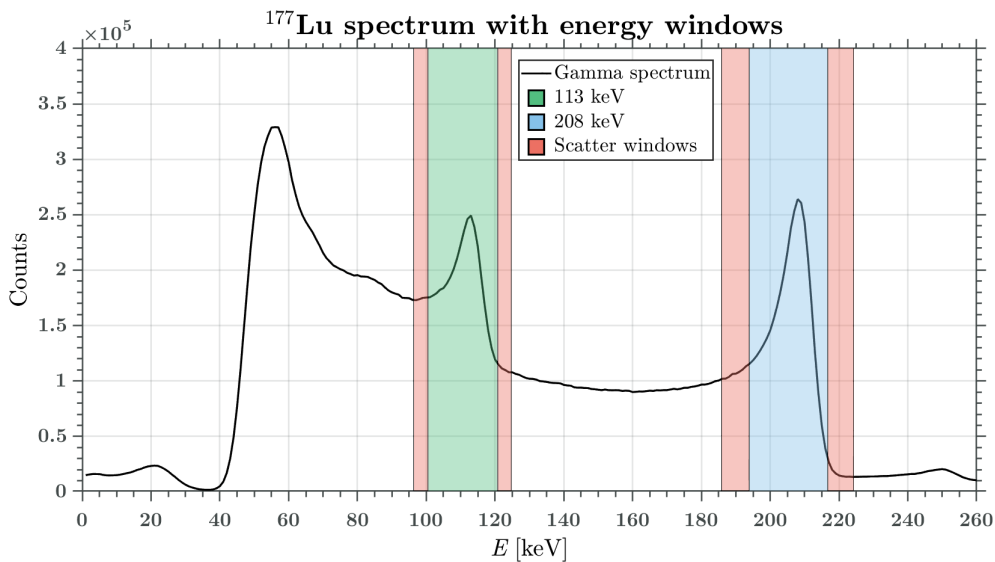
Figure 12: The figure shows two energy sessions, SG.Lu113B and SG.Lu208C, one for each peak of ^{177}Lu. The energy sessions shown are the most optimised ones of the energy sessions evaluated, as seen in table 5. The peak by 55 keV is not suitable for SPECT imaging.

4.2 Evaluation of prior weights for RDP and MRP

The results of the determination of equivalent prior weights for MRP and RDP are shown in figure 13 and 14. Additionally, the equivalent γ value for RDP is shown in figure 15.

The left column represents the SNR adjustment as function of β and γ for 360 ° CZT SPECT and the right column shows the same for Anger SPECT. All figures are plotted with the same y-axis range, to allow better visual comparison.
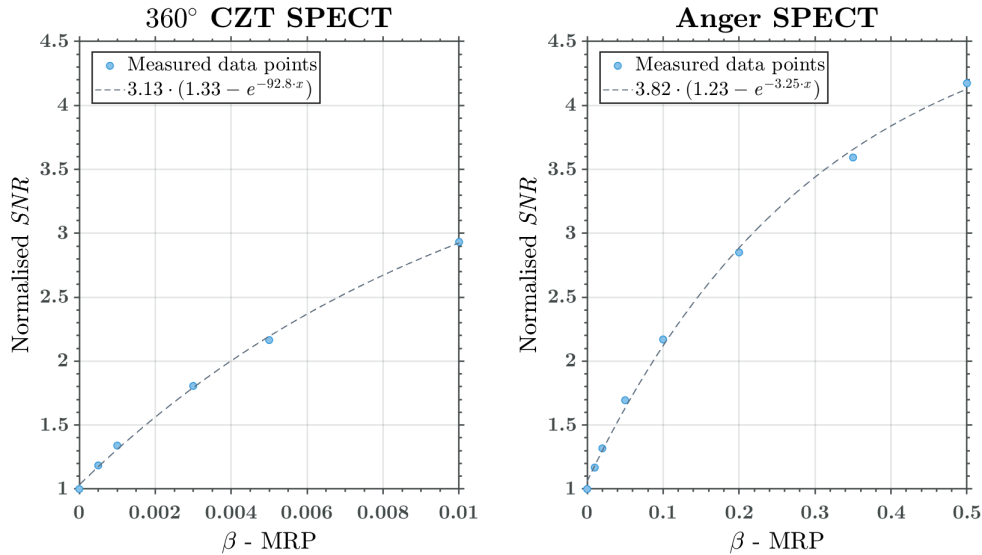
Figure 13: The figure shows the SNR improvement for both cameras as function of the Bayesian weight β for the Median Root Prior (MRP) reconstruction normalised to MAP-reconstruction with $\beta = 0$.
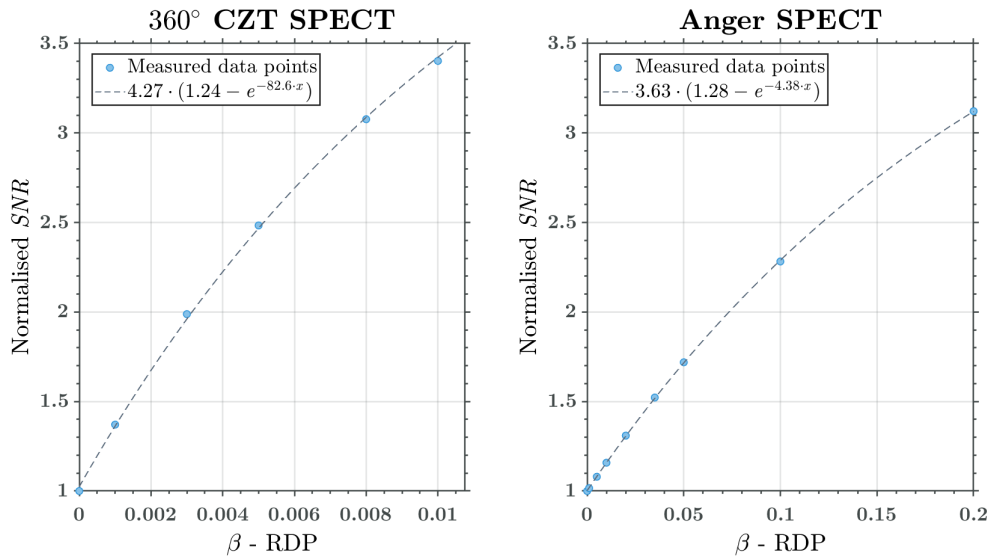
Figure 14: The figure shows the SNR improvement for both cameras as function of the Bayesian weight β for the Relative Difference Prior (RDP) reconstruction normalised to MAP-reconstruction with $\beta = 0$. For all data points γ is fixed to unity.
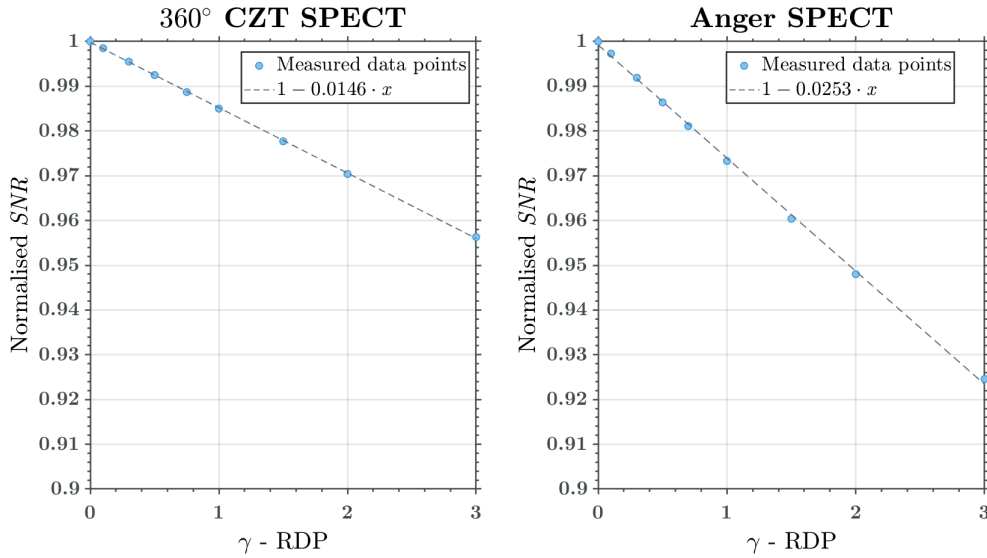
Figure 15: The figure shows the SNR adjustment for both cameras as function of the edge preservation constant γ for the Relative Difference Prior. For the 360° CZT SPECT β is fixed to 0.01 and for Anger SPECT β is fixed to 0.05 for all data points for each camera.

4.3 Variations of reconstructed signal depending on position in field of view on 360° CZT SPECT

4.3.1 Transaxial variations of reconstructed signal on 360° CZT SPECT

The variation of reconstructed signal within transaxial slices for ^{99m}Tc and both peaks of ^{177}Lu are shown in figures 16 A, B and C. The images show the sum of 10 transaxial slices which has been spatially filtered by convolution with a circular mean filter with a radius of 5 pixels. All pixel values has finally been normalised against the highest mean value. Both images for ^{177}Lu show distinct signal variations. In addition, the image for the 208-peak exhibits an increased signal in the anterior part of the FOV. The ^{99m}Tc image does likewise display some variations but these are not as apparent. Tables 6, 7 and 8 show the means of reconstructed signal for ^{99m}Tc, 208-peak of ^{177}Lu and 113-peak of ^{177}Lu, respectively, of 6 realisations of the 5 VOIs shown in figure 7. Figure 17 visualises the differences in means by showing box plots where all values of means have been normalised against the total mean. Consistently, the central and sinister VOIs display the lowest reconstructed signal. Furthermore, the anterior and posterior VOIs displays the highest reconstructed signal for the 208-peak while the posterior VOI also exhibits an equally high signal for ^{99m}Tc and the 113-peak of ^{177}Lu. Finally, table 9 shows the results of the ANOVA test with the null hypothesis that there are no statistical difference between the means in reconstructed signal of the different VOIs. The result show that there is a statistically significant difference in means of transaxial VOIs for ^{99m}Tc and the 208-peak of ^{177}Lu and thus the null hypothesis can be discarded for these. There was not a statistically significant difference in means between transaxial VOIs for the 113-peak of ^{177}Lu.

A   **B**   **C**
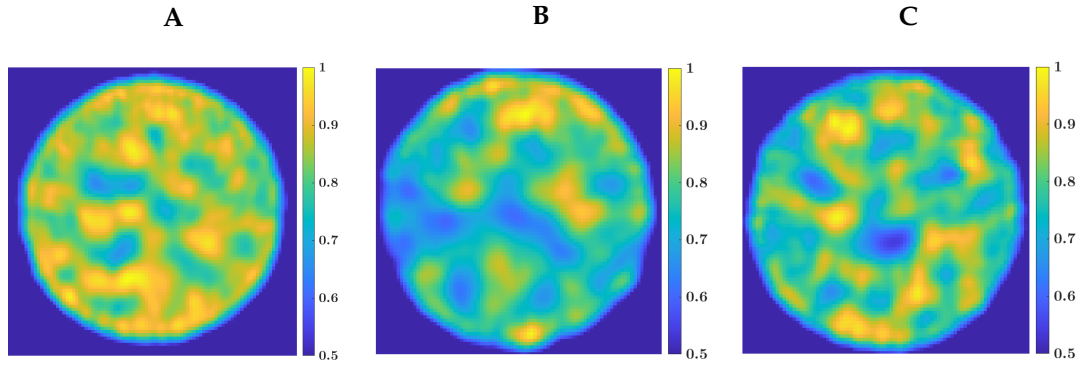
Figure 16: The figures shows the sum of 10 transaxial slices of the uniform Jaszczak filled with ^{99m}Tc (A), and ^{177}Lu using the 208-peak (B) and 113-peak (C) when using 360° CZT SPECT. The entire image is spatially filtered by convolution by a circular mean filter with a radius of 5 pixels. The result is normalised against the highest mean value.

Table 6: The table shows the average signals for ^{99m}Tc within transaxial VOIs anterior, sinister, central, dexter and posterior of the Jaszczak phantom as shown in figure 7 for 6 realisations.

VOI Position	Average ($\times 10^6$)	Variance ($\times 10^9$)
Anterior	1.09	1.1
Sinister	1.03	2.9
Central	0.995	1.4
Dexter	1.06	2.6
Posterior	1.09	2.4

Table 7: The table shows the average signals for the 208-peak of ^{177}Lu within transaxial VOIs anterior, sinister, central, dexter and posterior of the Jaszczak phantom as shown in figure 7 for 6 realisations.

VOI Position	Average ($\times 10^5$)	Variance ($\times 10^7$)
Anterior	2.06	3.6
Sinister	1.75	6.4
Central	1.81	11
Dexter	1.97	7.0
Posterior	1.87	2.0

Table 8: The table shows the average signals for the 113-peak of ^{177}Lu within transaxial VOIs anterior, sinister, central, dexter and posterior of the Jaszczak phantom as shown in figure 7 for 6 realisations.

VOI Position	Average ($\times 10^5$)	Variance ($\times 10^8$)
Anterior	2.54	4.4
Sinister	2.40	3.4
Central	2.34	5.6
Dexter	2.43	2.3
Posterior	2.59	1.9

Table 9: The table shows the result of the ANOVA tests with the null hypotheses that there are no significant difference between the means of the different transaxial VOIs for the different radionuclides and energies. The results are significant with $\alpha = 0.05$, except for the 113-peak of ^{177}Lu.

Radionuclide	p-Value
^{99m}Tc	4.40×10^{-3}
^{177}Lu- 208 keV	1.00×10^{-4}
^{177}Lu- 113 keV	1.59×10^{-1}

25
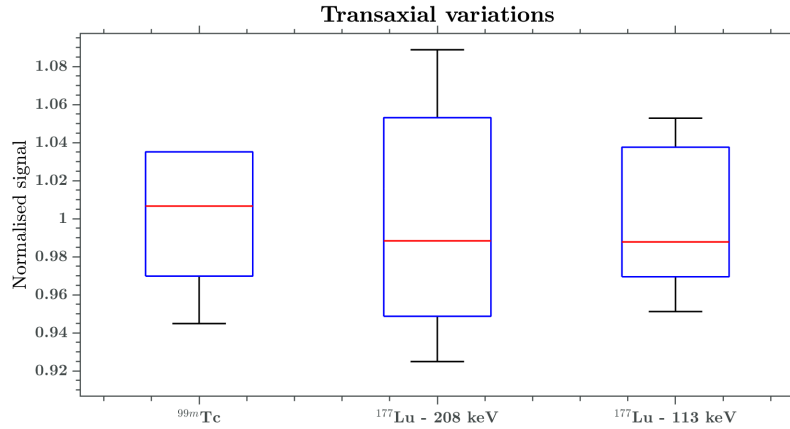
Figure 17: The figure shows box plots of the transaxial variations within the uniformly filled Jaszczak phantom in order to visually show the size of the differences between the different VOIs.

4.3.2 Axial variations of reconstructed signal on 360° CZT SPECT

The signal of the uniform phantom along the axial direction is shown in figure 18. The figure shows that both ^{177}Lu peaks exhibit distinct variations. The 208-peak in particular display a behaviour which appears symmetrical. The axial signal of ^{99m}Tc peak displays a comparatively stable behaviour. However, slices 35-45 display a distinct increase in signal compared to slices 50-60. Then, table 10, 11 and 12 shows the means of reconstructed signal for ^{99m}Tc, 208-peak of ^{177}Lu and 113-peak of ^{177}Lu- in that order - within 6 realisations of the 5 VOIs shown in figure 8. Figure 19 visualises the differences in means by showing box plots where all values of means have been normalised against the total mean. Consistently, just as for the transaxial VOIs, the central VOI displays the lowest reconstructed signal. Aside from this, no discernible pattern can be detected and claimed with certainty. Finally, table 13 shows the results of the one-way ANOVA tests. The results show that there is a statistically significant difference in means of axial VOIs for ^{99m}Tc as well as both peaks of ^{177}Lu.
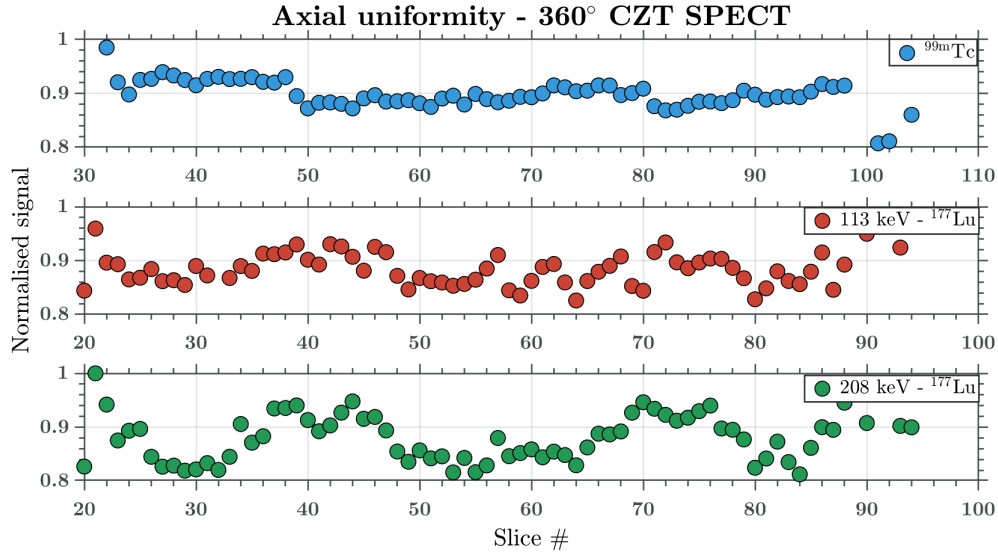
Figure 18: The figure shows the axial signal variation of ^{99m}Tc and both peaks of ^{177}Lu when using the 360 ° CZT SPECT. Each data point represent the total sum of a transaxial slice. This sum is plotted as function of axial slice position. All data has been normalised to the highest data point within each set. Note that the plot for ^{99m}Tc uses a different x-axis range. This is because this phantom was physically imaged in another position than the ^{177}Lu phantom.

Table 10: The table shows the average signals for ^{99m}Tc within axial VOIs caudal, inferior, central, superior and cranial of the Jaszczak phantom as shown in figure 8

VOI Position	Average ($\times 10^6$)	Variance ($\times 10^9$)
Caudal	7.1	3.1
Inferior	6.7	5.7
Central	6.7	5.8
Superior	6.9	1.2
Cranial	6.7	1.9

Table 11: The table shows the average signals for the 208-peak of ^{177}Lu within axial VOIs named caudal, inferior, central, superior and cranial of the Jaszczak phantom as shown in figure 8.

VOI Position	Average ($\times 10^6$)	Variance ($\times 10^8$)
Caudal	1.26	4.5
Inferior	1.28	3.6
Central	1.20	2.2
Superior	1.25	3.2
Cranial	1.27	7.5

Table 12: The table shows the average signals for the 113-peak of ^{177}Lu within axial VOIs named caudal, inferior, central, superior and cranial of the Jaszczak phantom as shown in figure 8.

VOI Position	Average ($\times 10^6$)	Variance ($\times 10^9$)
Caudal	1.68	1.3
Inferior	1.67	5.1
Central	1.58	2.9
Superior	1.64	2.9
Cranial	1.67	9.5

Table 13: The table shows the result of the ANOVA tests with the null hypotheses that there are no significant difference between the means of the different axial VOIs for the different radionuclides and energies. The results are significant with $\alpha = 0.05$.

| Radionuclide	p-Value
^{99m}Tc	1.83×10^{-7}
^{177}Lu- 208 keV	6.69×10^{-6}
^{177}Lu- 113 keV	1.16×10^{-2}
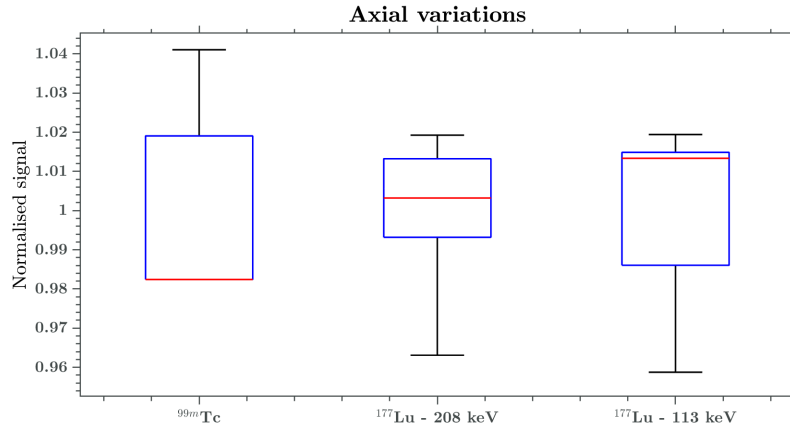
Figure 19: The figure shows box plots of the axial variations within the uniformly filled Jaszczak phantom in order to visually show the size of the differences between the different VOIs.

4.4 Measurements of single sphere in different geometries

4.4.1 Single sphere filled with ^{99m}Tc imaged in different positions

Table 14 shows the means of the delineated reconstructed signal of the 10 realisations of the ^{99m}Tc sphere in different parts of FOV while the sphere is placed in air. Table 15 shows the same for the sphere placed in water. Figure 20 shows the variations of all means of the sphere filled with ^{99m}Tc imaged in both an empty and water phantom background by normalising all value of means against the total mean. Two trends can be seen. The delineated reconstructed signal of the sphere placed in the anterior part of the FOV exhibits an increased signal compared to the rest. Moreover, the delineated reconstructed signal of the sphere placed in water is consistently higher than the same for the sphere placed in air. One exception should be noted, for the sphere placed in the anterior part of FOV, although the opposing difference here is very small. The results of the ANOVA tests, for both the sphere placed in air and water can be seen in table 16. The results show that there is a statistically significant difference in means of delineated reconstructed signal between the different sphere positions of ^{99m}Tc for both the sphere in air and water.

Table 14: The table shows the means of delineated reconstructed signal of 10 realisations of the sphere with ^{99m}Tc placed in 5 different positions of an empty phantom, shown in figure 9.

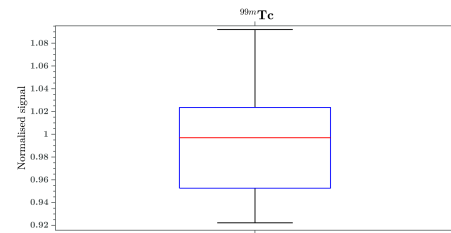| VOI Position	Average ($\times 10^4$)	Variance ($\times 10^5$)
Anterior	4.31	1.5
Sinister	3.75	1.8
Central	3.76	0.54
Dexter	3.82	1.8
Posterior	3.64	1.3

Table 15: The table shows the means of delineated reconstructed signal of 10 realisations of the sphere with ^{99m}Tc placed in 5 different positions of a water filled phantom, shown in figure 9.

VOI Position	Average ($\times 10^4$)	Variance ($\times 10^5$)
Anterior	4.30	1.9
Sinister	3.98	1.9
Central	3.95	1.1
Dexter	4.04	3.7
Posterior	3.92	1.9

Table 16: The table shows the result of the ANOVA tests with the null hypotheses that there are no difference in means of reconstructed signal between the sphere filled with ^{99m}Tc when imaged in the different positions shown in 9 The results are significant with $\alpha = 0.05$.

Phantom background	p-Value
Empty	8.51×10^{-38}
Water	1.94×10^{-17}

Figure 20: The figure shows a box plot visualising the variations of all spheres with ^{99m}Tc imaged in different positions, both with an empty and water filled background.

4.4.2 Single sphere filled with ^{177}Lu imaged in different positions using the 208-peak

Table 17 shows the means of the delineated reconstructed signal of the 10 realisations of the 208-peak of ^{177}Lu sphere in different parts of FOV shown in figure 9 while the sphere is placed in air. Table 18 shows the same for the sphere placed in water. Figure 21 shows the variations of all means of the sphere filled with ^{177}Lu, using the 208-peak when imaged both in an empty and water phantom background by normalising all value of means against the total mean. Just like for ^{99m}Tc, the same two trends can be seen. The delineated reconstructed signal of the sphere placed in the anterior part of the FOV exhibits an increased signal compared to the rest. Moreover, the delineated reconstructed signal of the sphere placed in water is consistently higher than the same for the sphere placed in air. In addition, the difference in means of delineated reconstructed signal between sphere positions dexter and sinister is noticeable. The results of the ANOVA tests, for both the sphere placed in air and water can be seen in tables 19. The result shows that there is a statistically significant difference in means of delineated reconstructed signal between the different sphere positions of the 208-peak of ^{177}Lu for both the sphere in air and water.

Table 17: The table shows the means of delineated reconstructed signal of 10 realisations of the sphere with the 208-peak of ^{177}Lu placed in 5 different positions of an empty phantom, shown in figure 9.

VOI Position	Average ($\times 10^3$)	Variance ($\times 10^4$)
Anterior	10.0	1.0
Sinister	9.43	1.7
Central	9.34	0.91
Dexter	9.77	0.62
Posterior	9.54	3.3

Table 18: The table shows the means of delineated reconstructed signal of 10 realisations of the sphere with the 208-peak of ^{177}Lu placed in 5 different positions of a water filled phantom, shown in figure 9.

VOI Position	Average ($\times 10^3$)	Variance ($\times 10^4$)
Anterior	10.6	2.6
Sinister	9.59	2.1
Central	9.96	6.4
Dexter	9.99	3.4
Posterior	9.61	2.4

Table 19: The table shows the result of the ANOVA tests with the null hypotheses that there are no difference in means of reconstructed signal between the sphere filled with ^{177}Lu using the 208-peak when imaged in the different positions shown in 9 The results are significant with $\alpha = 0.05$.

Phantom background	p-Value
Empty	2.86×10^{-16}
Water	1.94×10^{-17}

Figure 21: The figure shows a box plot visualising the variations of all spheres with ^{177}Lu using the 208-peak when imaged in different positions, both with an empty and water filled background.

4.4.3 Single sphere filled with ^{177}Lu imaged in different positions using the 113-peak

Table 20 shows the means of the delineated reconstructed signal of the 10 realisations of the 113-peak of ^{177}Lu sphere in different parts of FOV while the sphere is placed in air. Table 21 shows the same for the sphere placed in water. Figure 22 shows the variations of all means of the sphere filled with ^{177}Lu, using the 113-peak when imaged both in an empty and water phantom background by normalising all value of means against the total mean. Once again, the delineated reconstructed signal of the sphere placed in the anterior part of the FOV exhibits an increased signal compared to the rest. The trend of increased delineated reconstructed signal of the spheres in water is also apparent. The results of the ANOVA tests, for both the sphere placed in air and water can be seen in table 22. The result shows that there is a statistically significant difference in means of delineated reconstructed signal between the different sphere positions of the 113-peak of ^{177}Lu for both the sphere in air and water.

Table 20: The table shows the means of delineated reconstructed signal of 10 realisations of the sphere with the 113-peak of ^{177}Lu placed in 5 different positions of an empty phantom, shown in figure 9.

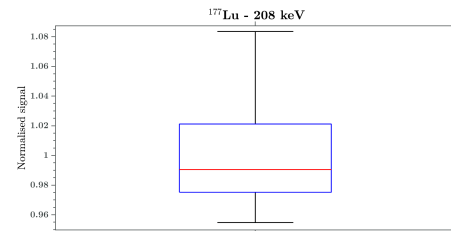| VOI Position	Average ($\times 10^4$)	Variance ($\times 10^4$)
Anterior	1.32	5.4
Sinister	1.28	6.2
Central	1.27	3.5
Dexter	1.27	3.4
Posterior	1.28	2.8

Table 21: The table shows the means of delineated reconstructed signal of 10 realisations of the sphere with the 113-peak of ^{177}Lu placed in 5 different positions of a water filled phantom, shown in figure 9.
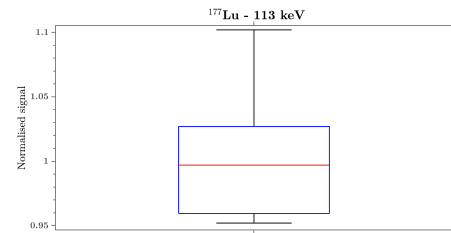
VOI Position	Average ($\times 10^4$)	Variance ($\times 10^5$)
Anterior	1.47	2.1
Sinister	1.35	0.62
Central	1.37	1.3
Dexter	1.39	1.5
Posterior	1.34	1.2

Table 22: The table shows the result of the ANOVA tests with the null hypotheses that there are no difference in means of reconstructed signal between the sphere filled with ^{177}Lu using the 113-peak when imaged in the different positions shown in 9 The results are significant with $\alpha = 0.05$.

Phantom background	p-Value
Empty	1.86×10^{-6}
Water	1.74×10^{-9}

Figure 22: The figure shows a box plot visualising the variations of all spheres with ^{177}Lu using the 113-peak when imaged in different positions, both with an empty and water filled background.

4.5 Measurements of point source with varying image FOV on 360° CZT SPECT

The results of the point source measurements of ^{99m}Tc and ^{177}Lu are shown in figure 23 and 24. The figures present the delineated reconstructed signal normalised against acquisition time for ^{99m}Tc and both peaks of ^{177}Lu with the impact of attenuation compensation and scatter compensation as well as penetration compensation for the 208-peak visualised. For ^{99m}Tc the reconstructed signal when using attenuation compensation and scatter compensation slightly decreases with FOV size for sizes Smallest, Small and Large but slightly increases again with size Largest.

For ^{177}Lu the trend is instead that the reconstructed signal slightly increases with FOV size for non compensated and attenuation compensated reconstructions, with size Largest being the obvious outlier. For the fully compensated reconstructions the reconstructed signal is constant for FOV sizes Smallest, Small and Large. Once again, the obvious outlier is size Largest.
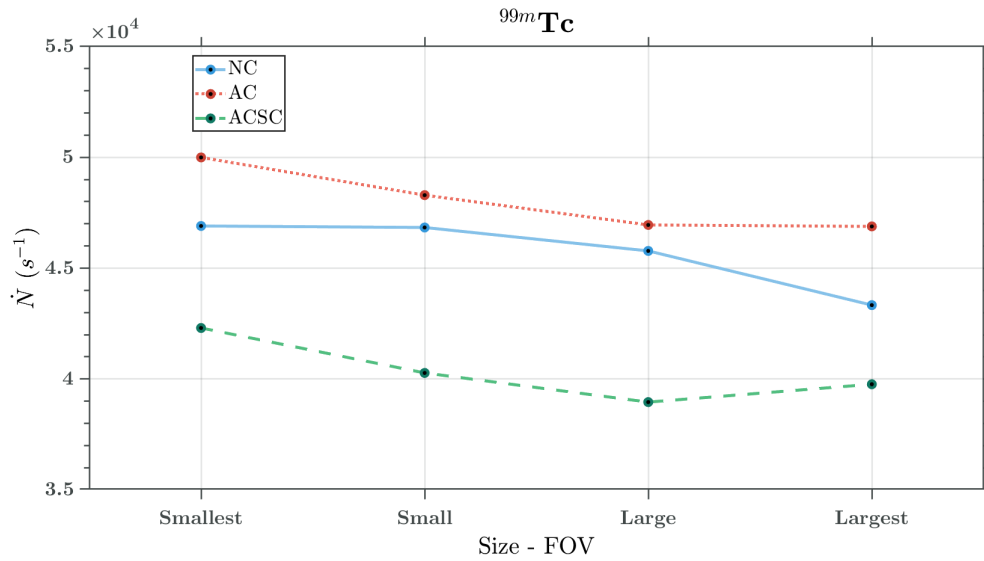
Figure 23: The figure shows the reconstructed signal of 4 point source measurements of ^{99m}Tc using different FOV sizes seen in figure 11. The point source is delineated with a spherical VOI with a radius of 5 cm. Results for OS-EM reconstructions with 15 iterations and 10 subsets are shown in three sets, one with compensation for attenuation and scatter, one with only the former and one without. All reconstructions are with resolution recovery.
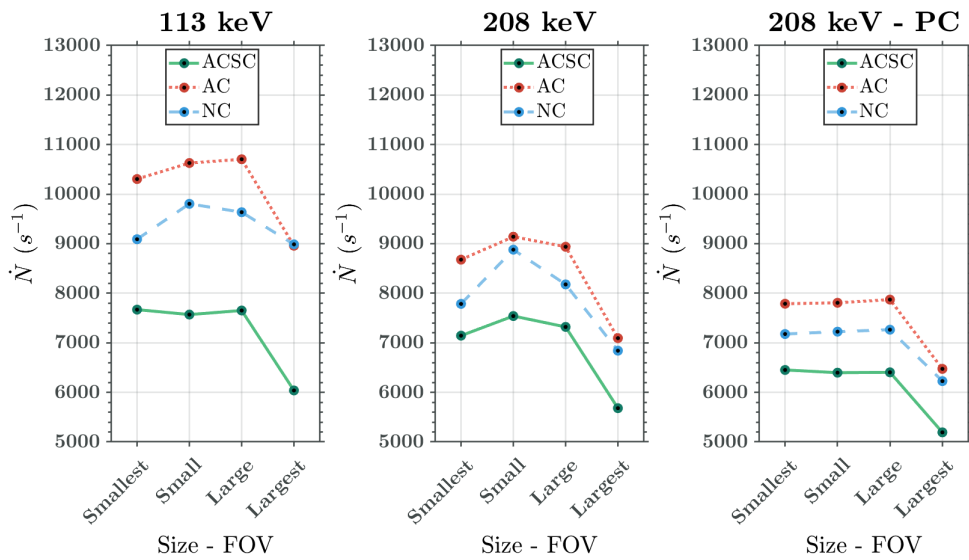
Figure 24: The figure shows the reconstructed signal of 4 point source measurements of ^{177}Lu using different FOV sizes seen in figure 11. The point source is delineated with a spherical VOI with a radius of 5 cm. Results for OS-EM reconstructions with 15 iterations and 10 subsets are shown in three sets, one with the 113-peak, one with the 208-peak without compensation for penetration and one with the 208-peak with penetration compensation. All reconstructions are with resolution recovery. AC, SC and PC denote attenuation compensation, scatter compensation and penetration compensation.

4.6 Comparison of image quality and activity quantification between $360°$ CZT SPECT and Anger SPECT

The result of the measured SNR:s for $360°$ CZT SPECT and Anger SPECT for the purpose of comparison is shown in tables 23 and 24. For 360 ° CZT SPECT all reconstructions but the images using the 208-peak have been made using a voxel size of 4.92 mm. This was not possible while using penetration compensation and therefore a voxel size of 2.46 mm was used for these and the resulting image was manually regridded to the larger voxel size. For Anger SPECT all reconstructions were made using a voxel size of 4.42 mm. The $360°$ CZT SPECT does overall exhibit a higher SNR than the corresponding images for Anger SPECT with the exception of the images with the 208-peak of ^{177}Lu which uses MRP and RDP. It is important to note that the Anger SPECT features a reconstruction using both ^{177}Lu peaks. As such, this is not comparable to the 113-peak reconstruction of the $360°$ CZT SPECT on even terms.

Table 23: The table shows the calculated SNR:s on the $360°$ CZT SPECT for the one ^{99m}Tc and two ^{177}Lu energy sessions, using the measurements of the uniform Jasczak phantom. The reconstructions for ^{99m}Tc and the 113-peak of ^{177}Lu were performed using a voxelsize of 4.92 mm while a voxel size of 2.46 mm was used for the 208-peak of [177]Lu. To compensate for this, this image matrix was regridded to a voxelsize of 4.92 mm before computation of SNR. The values are the means of SNR in three similar manually placed VOIs and the value within the parenthesis is the standard deviation of these.

Reconstruction method	SG.Tc	SG.Lu208C	SG.Lu113B
OS-EM	7.1(1)	4.0(1)	2.8(1)
BSREM-MRP	24(2)	7.42(1)	12(1)
BSREM-RDP	20(2)	6.82(1)	11(1)

Table 24: The table shows the calculated SNR:s on the Anger SPECT for the one ^{99m}Tc and two ^{177}Lu energy sessions, using the measurements of the uniform Jasczak phantom. All reconstructions were performed using a voxel size of 4.42 mm. The values are the means of SNR in three similar manually placed VOIs and the value within the parenthesis is the standard deviation of these. As it was not possible to reconstruct images on the Anger SPECT using only the 113-peak, the closest alternative which used both the 113-peak and the 208-peak was used.

Reconstruction method	Ang.Tc	Ang.Lu208	Ang.Lu208+113
OS-EM	6.50(1)	2.65(1)	3.35(3)
OSL-MRP	19.5(1)	7.77(1)	9.6(1)
OSL-RDP	13.2(1)	5.36(3)	6.8(1)

4.6.1 NEMA reconstructions with 360 ° CZT SPECT

Figure 25 shows examples of images of the NEMA phantom with ^{99m}Tc and ^{177}Lu using the 360° CZT SPECT. All reconstructions are made using 15 iterations and 10 subsets using resolution recovery with compensation for attenuation, scatter and penetration (208-peak).
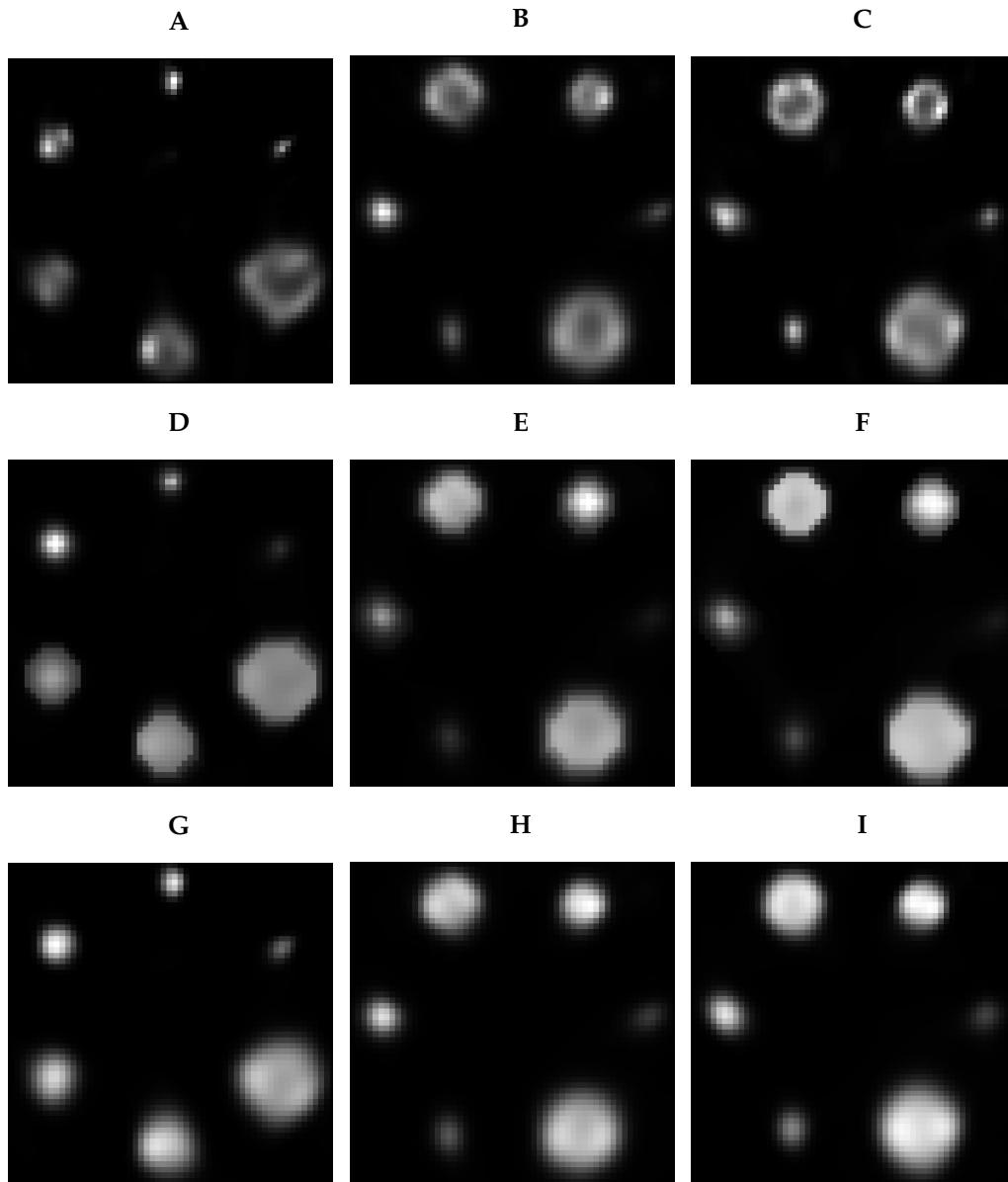
Figure 25: Reconstructions of the NEMA phantom using the 360 ° CZT SPECT filled with ^{99m}Tc (left column) and ^{177}Lu using the 208-peak (middle column) and the 113-peak (right column) Top row shows OS-EM reconstructions, middle BSREM-MRP and bottom BSREM-RDP. All reconstructions are done using 15 iterations and 10 subsets.

4.6.2 NEMA reconstructions with Anger SPECT

Figure 26 shows examples of images of the NEMA phantom with ^{99m}Tc and ^{177}Lu using the Anger SPECT. All reconstructions are made using 15 iterations and 10 subsets using resolution recovery with compensation for attenuation and scatter.
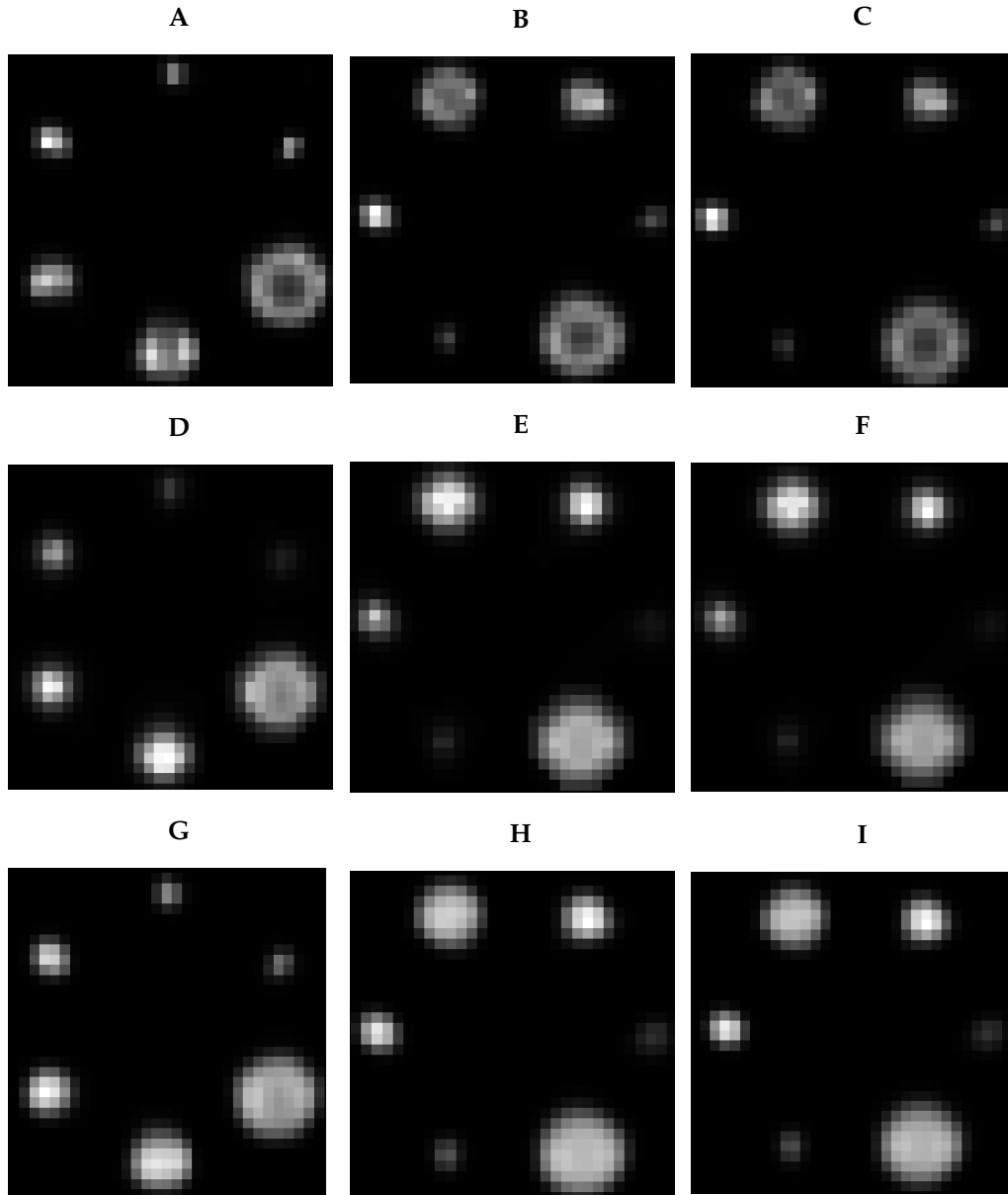
Figure 26: Reconstructions of the NEMA phantom using the Anger SPECT filled with ^{99m}Tc (left column) and ^{177}Lu using the 208-peak (middle column) and the 113-peak (right column). Top row shows OS-EM reconstructions, middle BSREM-MRP and bottom BSREM-RDP. All reconstructions are done using 15 iterations and 10 subsets with resolution recover and compensation for attenuation and scatter.

4.7 Calibration factors for activity quantification

The calibration factors for the two cameras when imaging ^{99m}Tc and ^{177}Lu are shown in table 25. The values presented in the table are computed as the mean of three measurements of the calibration factor, obtained by manually placing versions of the VOIs shown in figures 5 and 6.

Table 25: The table shows the determinated calibration factors for the two camera systems. The values in the fifth column represent the obtained calibration factor as the average of three values with the associated standard deviation, obtained by VOI placements in three image reconstructions using OS-EM, MRP and RDP.

Camera	Radionuclide	Energy Peak [keV]	Energy Session	Calibration factor $[\mathrm{s}^{-1}\,\mathrm{MBq}^{-1}]$
Anger SPECT	$^{99\mathrm{m}}\mathrm{Tc}$	140	Ang.Tc	88.4(1)
Anger SPECT	$^{177}\mathrm{Lu}$	208	Ang.Lu208	8.6(1)
Anger SPECT	$^{177}\mathrm{Lu}$	208+113	Ang.Lu208+113	15.4(1)
360° CZT SPECT	$^{99\mathrm{m}}\mathrm{Tc}$	140	SG.Tc	970(1)
360° CZT SPECT	$^{177}\mathrm{Lu}$	208	SG.Lu208C	80.2(2)
360° CZT SPECT	$^{177}\mathrm{Lu}$	113	SG.Lu113B	97.1(2)

4.8 Assessment of recovery curves

4.8.1 Recovery for $^{99\mathrm{m}}\mathrm{Tc}$

Figure 27, 28 and 29 show the recovery for spheres of different volume when filled with $^{99\mathrm{m}}\mathrm{Tc}$ for both camera systems. All reconstructions were made using 15 iterations and 10 subsets. The recovery of the spheres reconstructed with OS-EM is strictly higher for 360° CZT SPECT. However, the recovery varies in an unpredictable way. It shall be noted that the sphere with the highest recovery is the sphere with the second smallest volume and is seen as the sphere placed in the upper part of FOV, in figure 25:A. The recovery for Anger SPECT is consistently lower but follows a predictable pattern. The recovery for the reconstructions using MRP and RDP of the spheres filled with $^{99\mathrm{m}}\mathrm{Tc}$ exhibit trends akin to the one for OS-EM.

Figure 27: Recovery of $^{99\mathrm{m}}\mathrm{Tc}$ for 360° CZT SPECT and Anger SPECT as function of NEMA sphere volume. All reconstructions are made using OS-EM with 15 iterations and 10 subsets with resolutio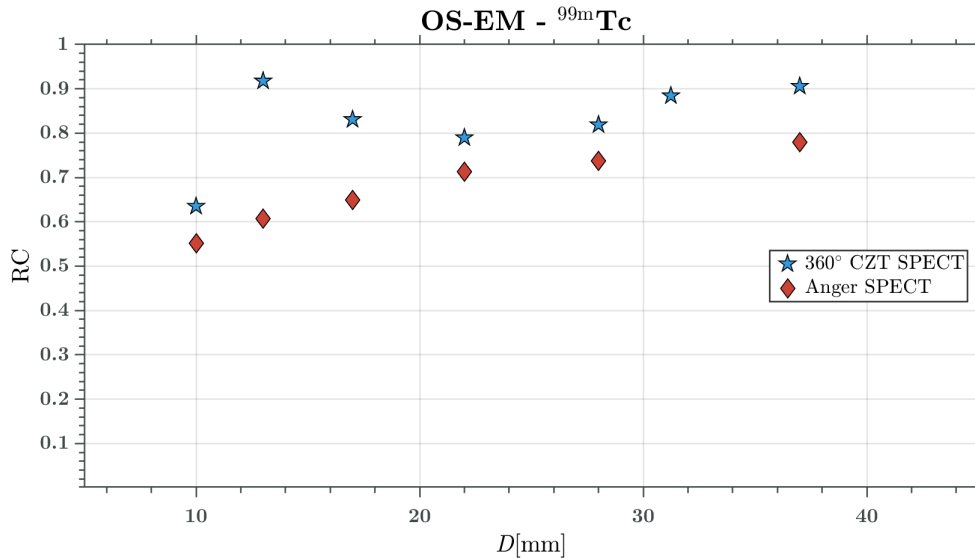n recovery and compensation for attenuation and scatter. The data for 360° CZT SPECT contains one extra data point which corresponds to the mean recovery of the single shere imaged in different positions within FOV.
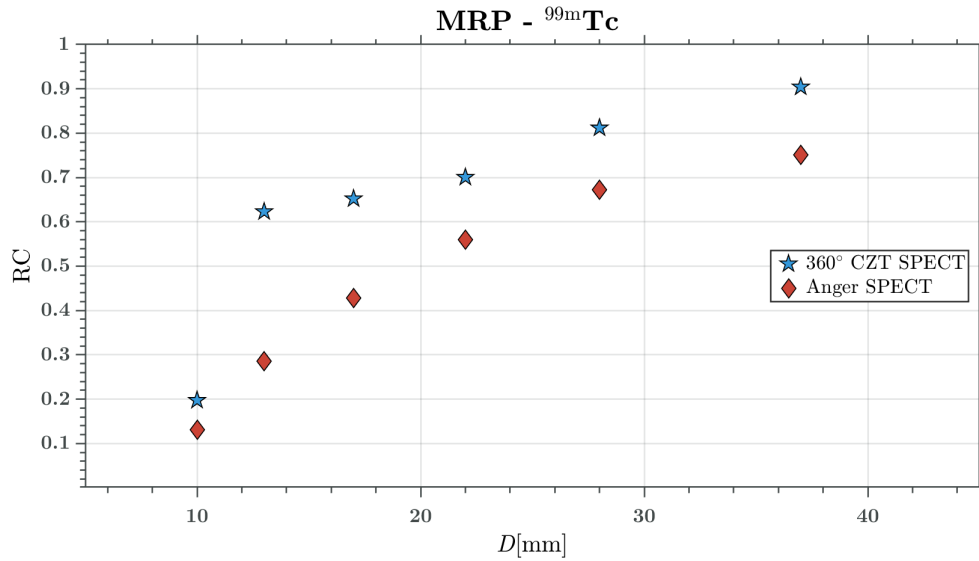
Figure 28: Recovery of ^{99m}Tc for 360° CZT SPECT and Anger SPECT as function of NEMA sphere volume. All reconstructions are made using MRP with β for an equivalent SNR-adjustment according to figures 13. MRP is implemented in BSREM for 360° CZT SPECT and OSL for Anger SPECT, using 15 iterations and 10 subsets with resolution recovery and compensation for attenuation and scatter.
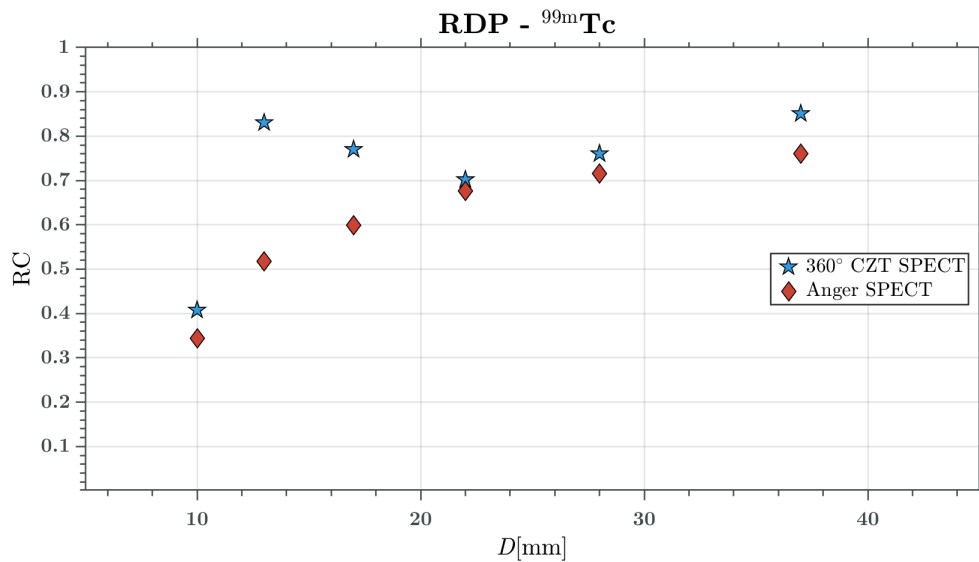
Figure 29: Recovery of ^{99m}Tc for 360° CZT SPECT and Anger SPECT as function of NEMA sphere volume. All reconstructions are made using RDP with β and γ for an equivalent SNR-adjustment according to figures 14 and 15. RDP is implemented in BSREM for 360° CZT SPECT and OSL for Anger SPECT, using 15 iterations and 10 subsets with resolution recovery and compensation for attenuation and scatter.

4.8.2 Recovery for 208-peak of ^{177}Lu

Figure 30, 31 and 32 show the recovery for spheres of different diameter when filled with ^{177}Lu, reconstructed with the 208-peak, for both camera systems. All reconstructions are made using 15 iterations and 10 subsets, with compensation for penetration with 360° CZT SPECT. It is not obvious which camera that exhibits the highest recovery when the 208-peak is used. However, the 360° CZT SPECT does, just like for ^{99m}Tc, show an unpredictable pattern where the recovery is unexpectedly high for spheres placed in the upper part of FOV, as seen in figure 25B, E and H. Once again, the recovery of the spheres in the images with Anger SPECT strictly increases with diameter.

Figure 30: Recovery of the 208-peak of ^{177}Lu for 360° CZT SPECT and Anger SPECT as function of NEMA sphere volume. All reconstructions are made using OS-EM with 15 iterations and 10 subsets with resolution recovery and compensation for attenuation and scatter. The data for 360° CZT SPECT contains one extra data point which corresponds to the mean recovery of the single shere imaged in different positions within FOV.
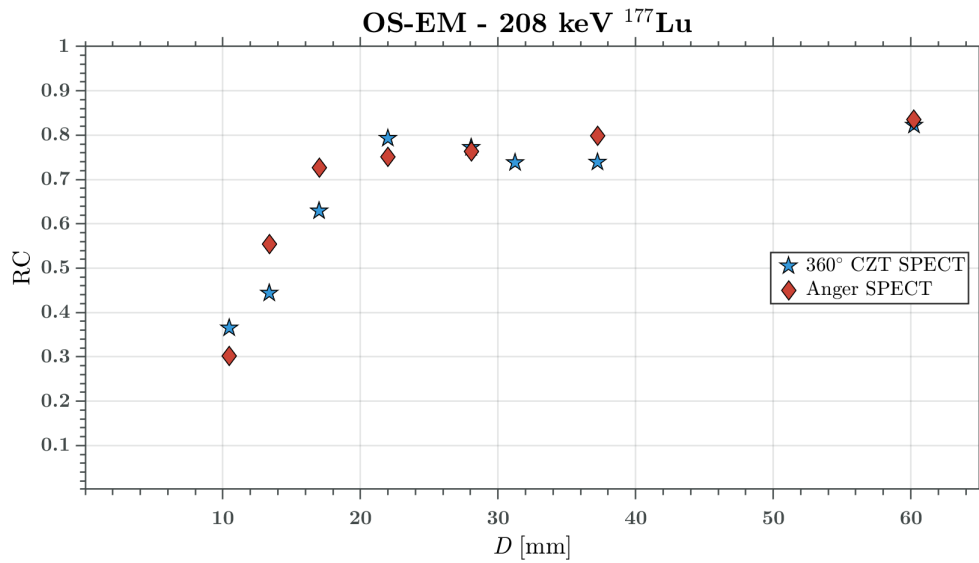

Figure 31: Recovery of the 208-peak of ^{177}Lu for 360° CZT SPECT and Anger SPECT as function of NEMA sphere volume. All reconstructions are made using MRP with β for an equivalent SNR-adjustment according to figures 13. MRP is implemented in BSREM for 360° CZT SPECT and OSL for Anger SPECT, using 15 iterations and 10 subsets with resolution recovery and compensation for attenuation and scatter.
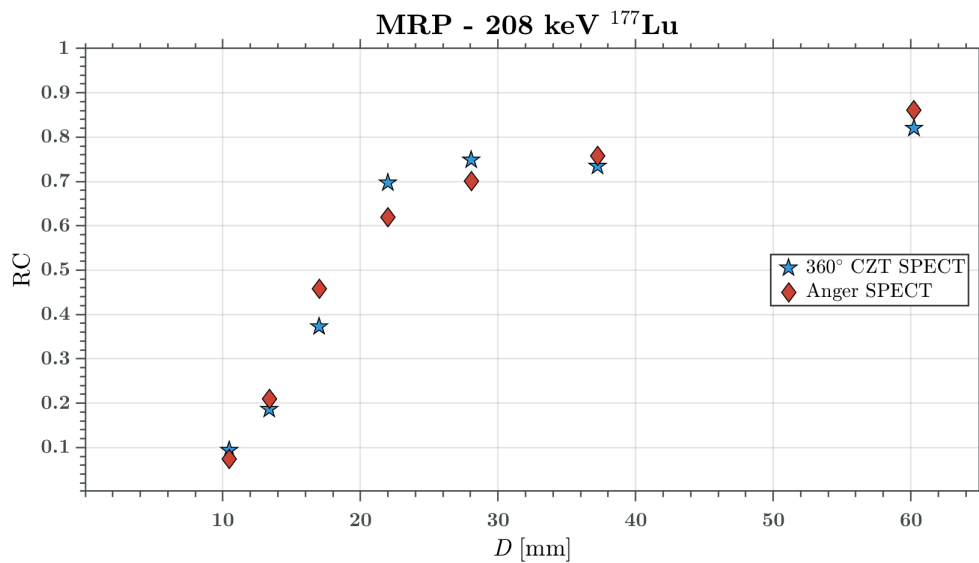
Figure 32: Recovery of the 208-peak of ^{177}Lu for 360° CZT SPECT and Anger SPECT as function of NEMA sphere volume. All reconstructions are made using RDP with β and γ for an equivalent SNR-adjustment according to figures 14 and 15. RDP is implemented in BSREM for 360° CZT SPECT and OSL for Anger SPECT, using 15 iterations and 10 subsets with resolution recovery and compensation for attenuation and scatter.
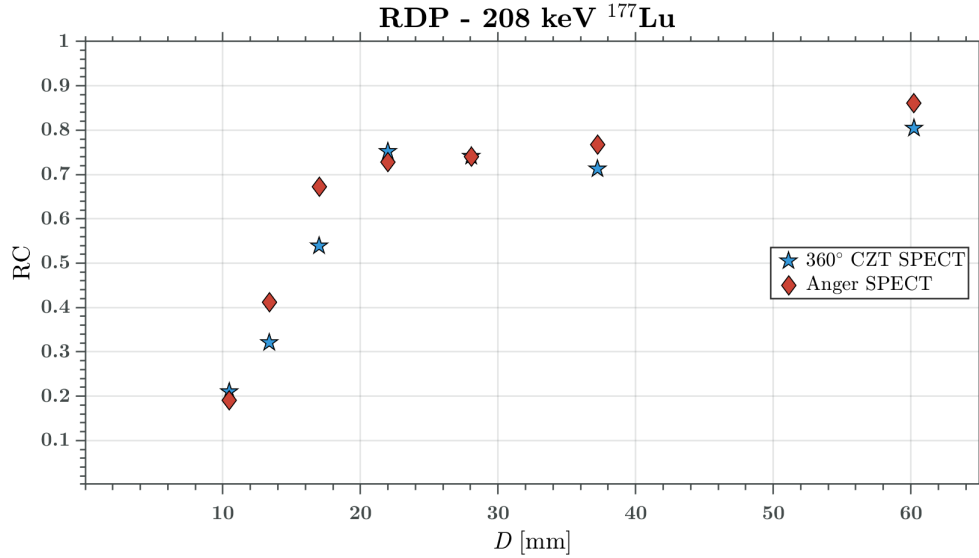
4.8.3 Recovery for 113-peak and dual peak of ^{177}Lu

Figure 33, 34 and 35 shows the recovery for spheres of different volume when filled with ^{177}Lu, reconstructed with the 113-peak, for 360° CZT SPECT and both peaks for Anger SPECT. All reconstructions are made using 15 iterations and 10 subsets. Here, the recovery for 360° CZT SPECT is mostly higher than for Anger SPECT, except for one sphere, but once again the spheres placed in the upper part of FOV, seen in figure 25C, F and I, display unexpectedly high recovery.

Figure 33: Recovery for 360° CZT SPECT and Anger SPECT as function of NEMA sphere volume. The former uses the 113-peak and the later uses both peaks for the reconstruction. All reconstructions are made using OS-EM with 15 iterations and 10 subsets with resolution recovery and compensation for attenuation and scatter. The data for 360° CZT SPECT contains one extra data point which corresponds to the mean recovery of the single shere imaged in different positions within FOV.
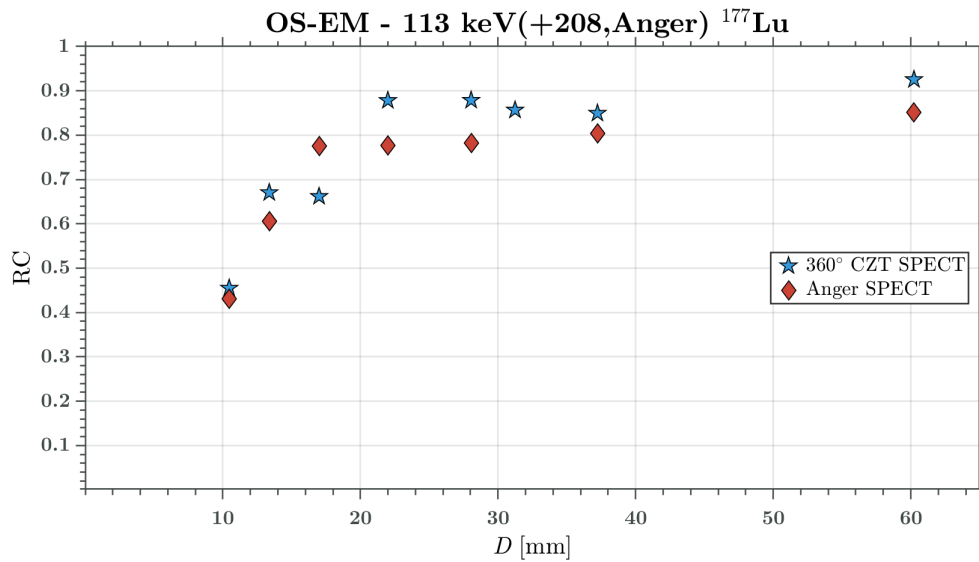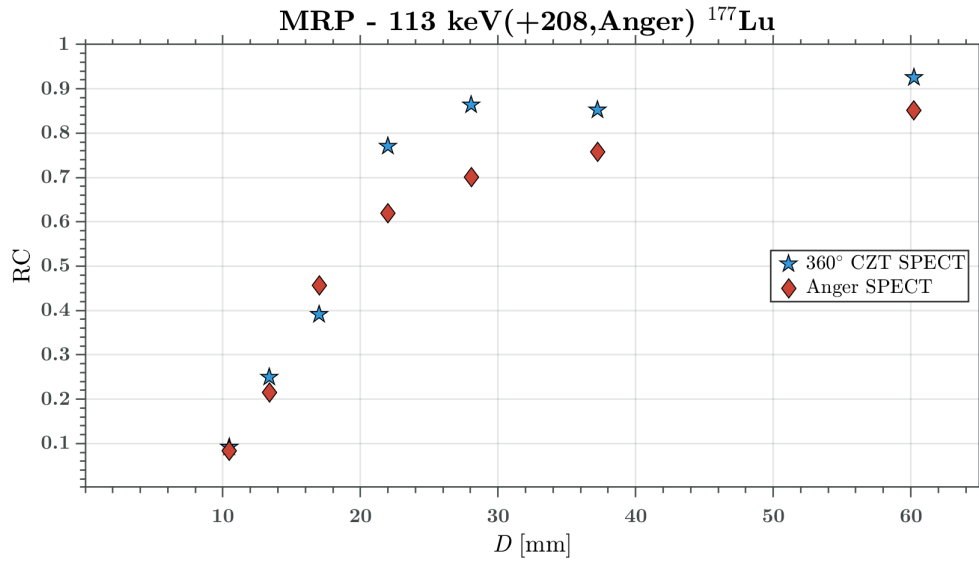
Figure 34: Recovery for 360° CZT SPECT and Anger SPECT as function of NEMA sphere volume. The former uses the 113-peak and the later uses both peaks for the reconstruction. All reconstructions are made using MRP with β for an equivalent SNR-adjustment according to figures 13. MRP is implemented in BSREM for 360° CZT SPECT and OSL for Anger SPECT, using 15 iterations and 10 subsets with resolution recovery and compensation for attenuation and scatter.
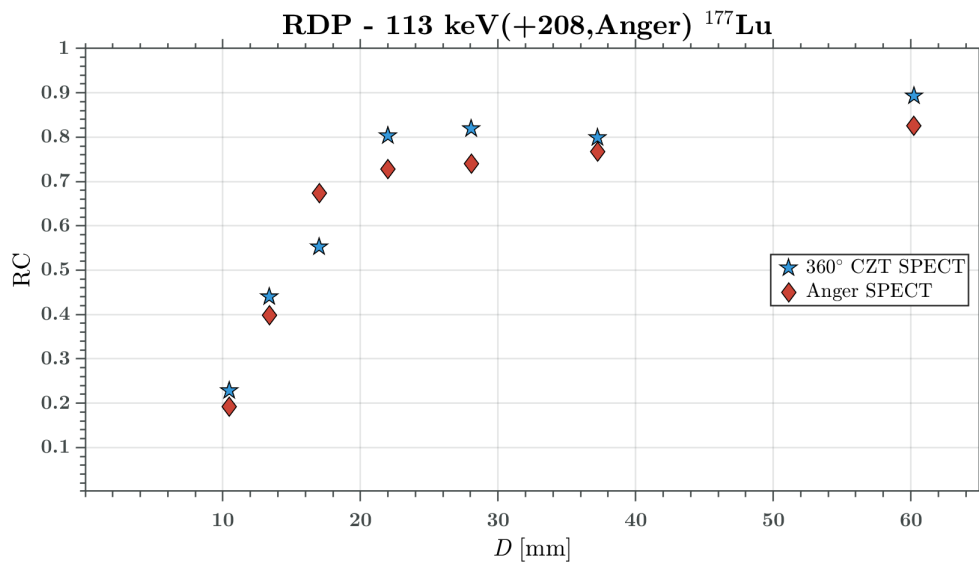
Figure 35: Recovery for 360° CZT SPECT and Anger SPECT as function of NEMA sphere volume. The former uses the 113-peak and the later uses both peaks for the reconstruction. All reconstructions are made using RDP with β and γ for an equivalent SNR-adjustment according to figures 14 and 15. RDP is implemented in BSREM for 360° CZT SPECT and OSL for Anger SPECT, using 15 iterations and 10 subsets with resolution recovery and compensation for attenuation and scatter.

5 Discussion

In this thesis, we have investigated a GE Starguide™, an example of a 360 CZT SPECT system and its use for activity quantification of ^{177}Lu. We have compared it to a GE NM/CT Discovery 670, a conventional Anger SPECT. We have compared the systems based on SNR, recovery and visual image quality. Additionally, we have investigated the dependency of the reconstructed signal on geometry when using the 360 CZT SPECT.

5.1 Choice and optimisation of energy sessions for reconstruction of ^{177}Lu images on 360° CZT SPECT

Two energy sessions, one for each peak of ^{177}Lu, were chosen to be the best, out of the energy sessions tested, for respective energy peak. These were energy sessions SG.Lu208C and SG.Lu113B. These energy sessions delivered the highest signal and the highest SNR for the reconstruction of the uniform Jaszczak phantom. It is however possible that alternative energy session which were not tried in this thesis would exhibit better results. Studying figure 12 it can be suspected that the upper scatter window of energy session SG.Lu208C does contain some primary photons, although it is debatable due to the energy resolution. If it is the case however, that would mean that the scatter compensation compensates for primary photons, which is not desirable. Similarly, the lower scatter windows of both energy sessions does indeed contain some primary photons due to the energy tailing effects of CZT detectors, which is an unavoidable attribute for the crystal. Hence, a scatter compensation method based on Monte Carlo simulated scatter would be preferable. Such a method would simulate the contribution in the projections from scatter and would therefore not be subject to the same issue as scatter compensation with DEW or TEW [53]. Additionally, a window based scatter compensation could introduce extra unwanted noise due to the addition or subtraction of noisy data in the scatter window to the already noisy energy window [54].

5.2 The dependency of the reconstructed signal on geometry with the uniform Jaszczak phantom

The method of adding 20 slices and performing convolution with a circular mean filter to transform the reconstructed images of the uniform Jaszczak phantom into the the representation seen in figure 16 should be noise resistant. Therefore, any variations seen in these images should uncover any systematic variations in reconstructed signal which could lead to a biased calibration factor should the images be used for determination of such a factor.

Despite the noise resistant filtering, variations in reconstructed signal of up to 30 % (for ^{99m}Tc), 40 % (for the 208-peak of ^{177}Lu) and 50 % (for the 113-peak of ^{177}Lu) can be seen in figure 16. In practice, it is unlikely that a VOI as small as the circular mean filter, used for convolution to construct the images illustrated in figure 16, would be used for determination of a calibration factor, meaning that the calibration factor would not be subject to that large of a bias as seen in the images.

However, variations of a more reasonable VOI, closer to the ones, used for determination of calibration factor, can be seen in tables 6, 7 and 8. It shows a statistically significant difference in reconstructed signal between VOIs of the uniform Jaszczak phantom, seen in figure 7 of up to 9 % (for ^{99m}Tc) and 18 % (for the 208-peak of ^{177}Lu). The difference in reconstructed signals for the 113-peak was not significant but similar trends with a maximum difference of 10 % can be seen.

The EANM practice guideline for quantitative SPECT-CT by Dickson et al. [55] stresses the importance of the accuracy of the calibration factor used for quantitative SPECT as errors in the factor leads to bias in the quantitative use of it. MIRD Pamphlet No. 26 by Ljungberg et al. [6] cites a number of phantom experiments evaluating the accuracy of quantitative SPECT of ^{177}Lu, the maximum being 15 % and several being sub- 10 % [56]. The use of the GE Starguide™ for activity quantification of ^{177}Lu would as such show a worse accuracy than the phantom experiments evaluated in the MIRD Pamphlet No. 26.

The axial variations in reconstructed signal of the uniform Jaszczak phantom, seen in figure 18 would also make quantitative SPECT on the system difficult as the calibration factor depending on the slices used, for the placement of the VOI used for determination of the calibration factor, could vary up to approximately 10 %, 15 % and 10 % for ^{99m}Tc, the 208-peak and 113-peak of ^{177}Lu respectively, when looking at figure 18. As we know, each of the detector columns consist of 7

modules of 16×16 elements. A periodicity of 16, especially for the 208-peak, could possibly be discerned in the figures but this is debatable.

5.3 Measurements of single sphere in different geometries

All the statistical tests of the measurements of the single sphere in different positions, both for the measurements in air and in water, show a significant difference in reconstructed signal as function of position within FOV. The trend is largely the same as for the transaxial variations of the uniform Jaszczak phantom. However, contrary to the separate tests for transaxial and axial variations of the uniform Jaszczak phantom it is not possible to decipher whether the variations of the reconstructed signal of the single sphere is because of transaxial or axial variations. This is because the imaging position of the sphere not only was varied transaxially but also axially. This axial movement was not regarded as important at the time of the measurements and therefore differs between the acquisitions. It is thus not taken into account in the statistical analysis of the reconstructed signal.

Regardless, the results serve well in demonstrating the possible variation in activity quantified in a e.g. tumour or a kidney, should the camera be used for activity quantification in a clinical setting of a patient treated for NETs with PRRT. Figure 21 shows a maximal difference in means of delineated reconstructed signal between sphere positions in a phantom, with water background, of about 10 %. In a clinical setting, this could on its own cause a 10 % difference in absorbed dose to the kidney, generally considered to be the dose-limiting organ in a PRRT [11]. This means that it is imperative to quantify the activity in the kidneys accurately and thus allowing the tumours to receive as many cycles of therapy as possible [57].

A trend that was not statistically tested for in the results is that of the difference in reconstructed signal between all reconstructions with the sphere in water and in air. For all but one single sphere position (anterior of ^{99m}Tc) the reconstructed signal of the sphere in each respective position is higher when placed in water. To add to the previous results, this is also a behaviour that could impact the accuracy of activity quantification negatively when using the 360° CZT SPECT.

5.4 Measurements of point source with varying image FOV of 360° CZT SPECT

From theory, we know that attenuation of photons lowers the count rate in a gamma camera, as seen in equation 3. It follows that the purpose of attenuation compensation is to increase the reconstructed signal to a level as if it was not affected by attenuation. Similarly, from theory we know that scattered photons increases the count rate in a gamma camera and contributes to a signal with no connection to the underlying activity. It follows then that the purpose of scatter compensation is to remove the contribution to the image from scatter, hence a scatter compensation lowers the reconstructed signal. This is exactly the trends that can be seen in figure 23 and 24 and this points towards the attenuation compensation and scatter compensation algorithms of the 360° CZT SPECT to work as intended.

The decline in reconstructed signal, seen in all curves in figure 23 and 24 as compensation for scatter is applied, is however quite large. It is expected that the reconstructed signal would decline, as the purpose of scatter compensation is to remove the contribution to the signal from photons that has undergone scattering that would give rise to counts with no connection to the real underlying activity distribution. However, the decrease in signal seems to be larger than expected, due to the lack of denser material than air within the FOV for photons to scatter against. Some contribution from scatter in the camera head and the collimator is expected but it is unlikely that this would be enough to explains this decline. As described in theory, the charge collection of CZT detectors is dependent on interaction position thus giving rise to energy-tailing effects. This can result in a spectrum where the primary photons are found in the scatter window used for scatter compensa-

tion. If this is not accounted for in the algorithm used for implementation of the window-based scatter compensation, it could result in the removal of primary photons from the reconstructed image. This is a potential disadvantage of window-based scatter compensation methods that a Monte Carlo-simulated method could account for [53][58]. A window-based scatter compensation method for quantitative SPECT require the identification or estimation of primary photons as detected within the scatter window [59].

The reconstructed signal as function of FOV size behaves reasonably close to what would be expected for ^{99m}Tc and sizes Smallest, Small and Large for ^{177}Lu. That is, a constant reconstructed signal no matter the FOV size. This indicates that the system compensates successfully for the sweeping motion of the detectors resulting in different fractions of detection time of the point source depending on FOV size. As mentioned in the results section the obvious outlier is size Largest for ^{177}Lu. It is possible that the measurement procedure was faulty, e.g. the point source changing position mid scan, resulting in an outlier. This is likely, given that the same size for ^{99m}Tc does not exhibit the same deviation. The fact that the remaining three sizes align so well to theory also makes this likely.

5.5 Comparison of quantitative image quality

The tables 23 and 24 show the computed SNRs of the images of the uniform phantom when imaged with the two camera systems, using OS-EM and Bayesian reconstructions with equal acquisition times, normalised for decay. As mentioned before, the voxel sizes used for reconstruction was matched as closely as possible in order to allow comparison of SNRs on even terms, when using the single VOI-based method to compute SNR. This meant that the 360° CZT SPECT images had to be reconstructed with a voxel size of 4.92 mm which did not support compensation for septal penetration, which the standard voxel size of 2.46 mm in contrast did. As compensation for septal penetration is a requirement to use for reconstructions of the 208-peak of ^{177}Lu, intended for activity quantification, this meant that these images had to be reconstructed using the standard voxel size and then regridded to 4.92 mm. However, this introduced another problem. The effect of MRP and RDP is heavily reliant on voxel size as they operate on a finite set of voxels. The impact on the image by MRP and RDP is higher, the larger the voxel size as the relative volume of the kernel used in the reconstruction becomes larger and thus the impact similarly becomes larger.

The different voxel sizes and the impact this had on the effect of MRP and RDP was not accounted for and therefore the SNR improvement from OS-EM to MRP or RDP is far higher for ^{99m}Tc and the 113-peak of ^{177}Lu compared to the 208-peak of ^{177}Lu for the 360° CZT SPECT. In retrospect, it may have been more fair to use another method to calculate SNR, one with a result that is not affected by voxel size. Nevertheless, the SNRs of 360° CZT SPECT is higher than the SNRs for Anger SPECT for ^{99m}Tc and the 208-peak of ^{177}Lu. This is indeed expected, given the reported higher sensitivity of the 360° CZT SPECT compared to conventional Anger cameras [43] [25].

The SNR of the dual peak of ^{177}Lu for Anger SPECT is higher than the SNR of the 113-peak of 360°CZT SPECT. This is however to be expected given the combined usable count rate is much higher for Anger SPECT when using both peaks. In contrast, what should be noted is that the SNR of the 113-peak of 360° CZT SPECT is higher than the SNR of the 208-peak for Anger SPECT. Given the lower physical yield of the 113-peak for ^{177}Lu compared to the 208-peak, this is notable.

The improvement in SNR by the Bayesian reconstructions is substantial. A slightly higher SNR for MRP compared to RDP is seen when using the Bayesian weights β, as presented in table 4. However, this could easily be modified by adjustment of the Bayesian weights β for both priors and the edge preservation constant γ for RDP.

5.5.1 Comparison of visual image quality

When inspecting the images of the NEMA-phantom with ^{99m}Tc and both peaks of ^{177}Lu, as seen in figures 25 and 26 it is evident that the voxel size of the Anger SPECT is larger than that of the 360° CZT SPECT - 4.42 mm compared to 2.46 mm. For the latter, this results in an image that appears more detailed compared to the equivalent image for the former.

Comparing the images of ^{99m}Tc and both peaks of ^{177}Lu reconstructed with OS-EM as seen in the first row for both figures it is striking that the spheres of the 360° CZT SPECT does not appear as spheres. This is evident in particular for the largest spheres for ^{99m}Tc and the 113-peak of ^{177}Lu. The same appearance is not present in the OS-EM images with Anger SPECT.

The reconstructions with OS-EM with both camera systems display the characteristic build-up of signal along the edges of the spheres and lower signal in the central region of the spheres which is typically associated with collimator response compensation artefacts as part of the resolution recovery algorithm [33].

The change of the visual quality of the images when using the Bayesian reconstructions is, just as the similar change in SNR, substantial. For MRP the biggest improvement of note is the smoother appearance of the spheres where the collimator response compensation artefact is decreased. However, the images with MRP on both camera systems exhibit another artefact where the spheres appear as polygons. This is especially evident for the 360° CZT SPECT, possibly because of the smaller voxel size. Furthermore, the smallest sphere of the NEMA body phantom, with a diameter of 10 mm, is visually indistinguishable with the gray-level map used. This is not unexpected as the impact of MRP on objects smaller than the kernel used for computation of the median root making it impossible to resolve the underlying distribution, is known [60]. The images reconstructed with RDP achieves the same noise reducing effect such as MRP where the collimator response compensation artefact is reduced and the spheres appear more uniform.

5.6 Recovery as function of sphere diameter

The recovery curves with ^{99m}Tc and the 208-peak and dual peak of ^{177}Lu follow an expected pattern for Anger SPECT. The recovery is strictly increasing as the diameter of the sphere increases. Furthermore, the recovery appears to approach unity as the diameter approaches infinity which is to be expected. Perhaps, it could be argued that the recovery of the spheres with diameters 13 mm and 17 mm for both ^{177}Lu recovery curves possibly are higher than what would be expected when comparing these to the recovery of the other spheres. This effect is however small and of minor importance.

The recovery curves with ^{99m}Tc and the 208-peak and 113-peak of ^{177}Lu for 360° CZT SPECT does not follow the same pattern. In particular, in figure 27 the sphere with a diameter of 13 mm displays the highest recovery of all spheres, even higher than the sphere with a diameter of 37 mm. This is unexpected. Had the same phantom not been imaged in the Anger SPECT and yielded the recovery curve as discussed in the previous paragraph it would have been easy to blame the unexpected behaviour on poor preparation of the phantom. As this is clearly not the case, the source of the unexpected behaviour must be somewhere in the reconstruction process of the 360° CZT SPECT. Similarly, for both peaks of ^{177}Lu the spheres with diameters 22 mm and 28 mm exhibit higher recovery than the two subsequent spheres with higher diameter.

When studying figure 25 one may note that the spheres highlighted above, the one with a diameter of 13 mm for ^{99m}Tc and the ones with diameters of 22 mm and 28 mm for ^{177}Lu are positioned in the upper part of the FOV when imaged. Therefore, it is easy to attribute this to the previous results of the tests of the positional dependency of the reconstructed signal of the 360° CZT SPECT where it was seen that there is a significant difference in delineated reconstructed signal for a sphere placed in different parts of the FOV. Furthermore, as seen in the tables in the section describing the

measurements of the single sphere imaged in different FOV positions, it is generally the sphere placed in the anterior part of the FOV which displays the highest reconstructed signal. It is plausible that this is the reason for the unexpected behaviour of the recovery of the 360° CZT SPECT and the unexpectedly high recovery of the sphere and spheres imaged in the anterior part of the FOV.

The recoveries using OS-EM for ^{99m}Tc and both peaks of ^{177}Lu, shown in figure 27, 30 and 33 all contains one extra data point, with a diameter of 32 mm, compared to the rest. This recovery data point represents the mean of the recovery of the same sphere when it was placed in different FOV positions. Only the measurements of the sphere placed in water was used since all other recovery data points similarly originates from spheres imaged in water. However, it shall be noted that this resulted in a higher recovery than if the measurements of the sphere placed in air also was used, as the signal of the spheres placed in water was obviously higher, as previously discussed. However, the recovery of this sphere should serve as a data point where the impact of the positional variation of delineated reconstructed signal is minimised, by the act of averaging the different recoveries.

Overall, the recovery - possibly except for the 208-peak - is higher when using the 360 ° CZT SPECT compared to Anger SPECT, even when taking the unstable pattern into consideration. This is expected due to the close distance acquisition that the detector configuration allows, resulting in a theoretical higher resolution than for Anger SPECT. For the 113-peak the effect is the highest. It is plausible that this is an effect of using a LEHR collimator compared to the Anger SPECT which used a MEGP collimator for ^{177}Lu. In return, it is plausible that the added contribution of septal penetration for the 208-peak resulted in a lower recovery for the 208-peak compared to the 113-peak.

5.6.1   The recovery with MRP and RDP

The expectation with Bayesian reconstruction using priors such as MRP and RDP is to increase SNR while retaining the comparably high recovery that OS-EM without post-filtration achieves. However, there is a visible negative impact on the recovery compared to the recovery of OS-EM when using MRP and RDP. This is particularly evident for the recovery of the spheres with a small diameter when using MRP, where the recovery for the small spheres are close to zero. As previously mentioned in the section on the visual interpretation of the reconstructed images using MRP, the disability for objects smaller than the kernel size to converge is a known property of MRP [60]. However, in contrast, as the spheres become very large the recovery with MRP begins to approach that of OS-EM and even surpasses it.

The recovery with RDP is also lower than the recovery with OS-EM for the small spheres although not nearly as low as MRP. In contrast, the recovery is still usable for the small spheres. For the bigger spheres there is a noticeable decline in recovery for RDP compared to OS-EM, although slight. Overall, the recovery with RDP is usable for all sphere volumes while the same cannot be said for MRP.

5.7   Reasons for the unexpected behaviour of 360° CZT SPECT

We have now demonstrated that the GE Starguide™ used with Smartconsole version 1.6.0 does exhibit a number of different issues that potentially affects its applicability for quantitative SPECT. A list of these issues is found below.

1. A significant variation in reconstructed signal in a uniform phantom as function of position in FOV in transaxial direction for ^{99m}Tc and the 208-peak of ^{177}Lu, seen in figure 16, 17 and tables 6-9.

2. A significant variation in reconstructed signal in a uniform phantom as function of position

in FOV in axial direction for ^{99m}Tc and both peaks of ^{177}Lu, seen in figure 18, 19 and tables 10-13.

3. A significant variation in delineated reconstructed signal of a sphere imaged in different parts of the FOV for ^{99m}Tc and both peaks of ^{177}Lu, seen in tables 14-22 and figures 20, 21 and 22.

4. An obvious difference between measurements where the delineated reconstructed signal of a sphere is increased by about 10 % for measurements where the sphere is placed in a water phantom background compartment, compared to where the sphere is placed with the phantom background compartment empty for ^{99m}Tc and both peaks of ^{177}Lu, seen in tables 14-22.

5. An unexpectedly large decrease in delineated reconstructed signal of a point source as scatter compensation is applied, seen in figure 23 and 24.

The reason for all these unexpected results is not known. It is also not known whether the same reason is the source of all these discrepancies or if there are several issues contributing.

As a consequence of these unexpected results, a meeting has been held with the engineering team at GE Healthcare, the manufacturer of the system. The purpose of this meeting was to present and discuss reasons for the unexpected results when using the GE Starguide™. Some possible sources of error, discussed below, was raised during this meeting.

For the 208-peak of ^{177}Lu an increase in reconstructed signal in the upper part of the FOV is expected for a reconstruction not subjected to penetration compensation. This is because the probability for septal penetration is increased with lower source-to-collimator distance [17]. Therefore, as the design of the 360° CZT SPECT allows individual detectors to come very close to the upper part of the phantom contrary to the lower part of the phantom where the bed disallows close contact of the phantom and the detectors, a higher signal in the upper part of the FOV is expected for the 208-peak reconstructed without septal penetration. However, given that penetration for septal penetration was used, this effect should be compensated for. Given the fact that a similar trend can be seen for ^{99m}Tc and the 113-peak of ^{177}Lu it is likely that the penetration compensation is satisfactory and that the source for the unexpected results is the same.

A source for issues 1, 2 and 3 could be related to the sweeping motion of the detectors of the system. Due to this motion, a given source of activity represented by a voxel in the FOV, is not positioned perpendicularly to the collimator surface during the entire scan thus decreasing the time detector is facing a source, the further the source is from the detector. Incomplete compensation for this in the software could explain this variation in reconstructed signal.

Another possible source of issues 1, 2 and 3 was raised in the meeting with the engineering team of GE Healthcare. It was discussed whether the continuous sweeping motion of the detectors across the FOV is at fault. As this happens, the data is binned into different discrete projections. This is done by averaging of the data across angular intervals. The further the source-to-collimator distance, the spatial distance between the edges of the angular interval that the detector sweeps across and the angle of the bin that the data is collected to is increased. If this is the reason for the errors, it would be solved by using the camera in step and shoot mode. This has not been done during this work but would be the next step in investigating this.

Errors 4 and 5 are related due to the likely reason for both being the scatter compensation. For error 5 it is likely that the source of error is the scatter compensation subtracting primary photons from the energy window due to the energy tailing effects. The measurements of the single sphere imaged in different positions of the FOV where the sphere was placed in an empty phantom background does not include a lot of material causing a contribution to detected scattered photons compared to the similar measurement with a water phantom background. In the meeting with GE Healthcare, it was reported that the system in its current form does estimate a subset of the photons within the scatter windows for the 208-peak of ^{177}Lu to be primary, meaning that the scatter

compensation does not remove the signal from primary photons within the main energy window. This is however as of Smartconsole version 1.6.0, not implemented for the 113-peak of ^{177}Lu nor for ^{99m}Tc. Therefore, the large decrease in signal as scatter compensation is applied is explained for the 113-peak of ^{177}Lu and for ^{99m}Tc. It also plausibly explains the increase in delineated reconstructed signal for the measurements in phantom background with water compared to without water due to the lack of material in the FOV, contributing to scatter. However, despite the implementation of estimation of primary photons in the scatter window for the 208-peak this similar trend can be seen.

5.8   Limitations and future outlook

Only one camera of each type was used in this thesis. As it is possible that the performance of single cameras could vary it would have been desirable to do some measurements on the same camera models, placed elsewhere. This is especially true for the GE Starguide™ as issues with it was found. The particular specimen of this camera that was used, is merely 1 year old and it is possible that only this specimen has the issues found in this thesis.

The possibility of reconstructing a ^{177}Lu image using both the 113-peak and the 208-peak has been a marketed ability of the GE Starguide™. However, this feature has not as of the time of writing been implemented on the system. However, once it is introduced, it should promise increased image quality and more precise recovery.

It is important to note that this thesis has only shown the existence of issues that make the usability of the GE Starguide™ for activity quantification uncertain. It has not shown any reasons for the behaviour. Therefore, the next step would be to conduct experiments with the purpose of finding the reason for the issues. As described earlier, a first step to this would be to remake acquisitions using step and shoot mode rather than continuous mode.

Another interesting prospect would be to model the dependence of the reconstructed signal on geometry. This could be done by three-dimensionally mapping the response of a single sphere placed in the entire FOV of the camera and normalising the result against the mean of all acquisitions. If this result was repeatable and even reproducible on all Starguide™ systems a correction matrix could be introduced that could be used for compensation of all subsequent measurement. Unfortunately, this would be a dauntingly hefty and cumbersome task and would require a robotic system for exact positioning.

On a positive note, there has been communication with GE Healthcare on the results in this thesis. As a result all list files acquired and used during the thesis has been shared with them for analysis. If the reason for the issues found is located in the software, it is possible that this could aid GE Healthcare in finding a solution to the issues and implement this on all their systems.

6   Conclusions

In this work, the feasibility of a 360° CZT SPECT for activity quantification of ^{177}Lu has been compared to a Anger-based SPECT using activity quantification of ^{99m}Tc as a baseline. It has been done by the measurement of various phantoms in different phantom geometries. The results show that there is a significant variation in reconstructed signal as function of position in the FOV for the 360° CZT SPECT for ^{99m}Tc and both energy peaks of ^{177}Lu. It manifests itself as an unstable calibration factor for activity quantification and make the camera's use for activity quantification inaccurate. Compared to Anger-SPECT, the camera does however show a higher quantitative image quality and an overall higher recovery, although unstable. This makes the results for the 360° CZT SPECT promising should the reason for the positional unstability of the reconstructed signal be found and solved.

7   Acknowledgements

I would like to express my deepest gratitude to my supervisors for making this semester such a fun and worthwhile one!

- **Anna Stenvall**, thank you for your endless support, encouragement, and guidance along the way! Special thanks for helping me with the phantom measurements even during evenings and your designated day off!

- **Johan Gustafsson**, thank you for your invaluable expertise on everything from mathematical statistics to resolution compensation to english grammar! I am grateful for your willingness to answer my questions, which have enriched my understanding of these subjects!

- **Erik Larsson**, thank you for your innovative ideas and for your expertise on the conventional Anger camera! I am grateful for your assistance in planning the phantom measurements, which played a crucial role in the success of this project.

Additionally, I would like to thank **Irma Cerić Andelius**, **Michael Ljungberg**, **Elias Nilsson**, **Lena Jönsson** and **Martin Plate** for their contribution, major or minor, to the project.

I would also like to thank my friends back at Fysicum, in the Zångo research group, as well as my friends here at the Medical Radiation Physics department for these 5 years. Without you, it would not have gone as smooth, nor have been as fun as it has been.

Finally, I would like to thank my family for always being there.

References

[1] Anna Sundlöv. "Tailoring Radionuclide Therapy of Neuroendocrine Tumors - Bridging The Gaps". Dissertation. Lund: Lund University, Faculty Of Medicine, 2020.

[2] Ute Hennrich and Klaus Kopka. "Lutathera®: The first FDA- and EMA-approved radiopharmaceutical for peptide receptor radionuclide therapy". In: *Pharmaceuticals* 12.3 (2019), p. 114. DOI: 10.3390/ph12030114.

[3] Ema. *Pluvicto*. Apr. 2023. URL: https://www.ema.europa.eu/en/medicines/human/EPAR/pluvicto.

[4] Ute Hennrich and Matthias Eder. "[177lu]lu-PSMA-617 (pluvictotm): The first FDA-approved radiotherapeutical for treatment of prostate cancer". In: *Pharmaceuticals* 15.10 (2022), p. 1292. DOI: 10.3390/ph15101292.

[5] Louise Emmett et al. "Lutetium177PSMA radionuclide therapy for men with prostate cancer: A review of the current literature and discussion of practical aspects of therapy". In: *Journal of Medical Radiation Sciences* 64.1 (2017), pp. 52–60. DOI: 10.1002/jmrs.227.

[6] Michael Ljungberg et al. "Mird pamphlet no. 26: Joint EANM/MIRD Guidelines for quantitative 177lu spect applied for dosimetry of radiopharmaceutical therapy". In: *Journal of Nuclear Medicine* 57.1 (2015), pp. 151–162. DOI: 10.2967/jnumed.115.159012.

[7] *Quality Assurance for Radioactivity Measurement in Nuclear Medicine*. Technical Reports Series 454. Vienna: INTERNATIONAL ATOMIC ENERGY AGENCY, 2006. ISBN: 92-0-105306-1. URL: https://www.iaea.org/publications/7480/quality-assurance-for-radioactivity-measurement-in-nuclear-medicine.

[8] Collie Miller, Larry Filipow, and Stuart Jackson. "A Review of Activity Quantification by Planar Imaging Methods". In: *Journal Of Nuclear Medicine* 23.1 (1995).

[9] Bin He and Eric C Frey. "The impact of 3D volume of interest definition on accuracy and precision of activity estimation in quantitative SPECT and Planar Processing Methods". In: *Physics in Medicine and Biology* 55.12 (2010), pp. 3535–3544. DOI: 10.1088/0031-9155/55/12/017.

[10] F.G. KONDEV. "Nuclear Data Sheets for A=177". In: *Nucl Data Sheets (NY NY)*. Vol. 98. 2003, pp. 801–1095.

[11] Katarina Sjögreen Gleisner et al. "EANM Dosimetry Committee recommendations for dosimetry of 177LU-labelled somatostatin-receptor- and PSMA-targeting ligands". In: *European Journal of Nuclear Medicine and Molecular Imaging* 49.6 (2022), pp. 1778–1809. DOI: 10.1007/s00259-022-05727-7.

[12] E. BROWNE and J. K. TULI. "Nuclear Data Sheets for A=99". In: *Nucl Data Sheets (NY NY)*. Vol. 145. 2017, pp. 25–340.

[13] Won Woo Lee. "Clinical applications of technetium-99m quantitative single-photon emission computed tomography/computed tomography". In: *Nuclear Medicine and Molecular Imaging* 53.3 (2019), pp. 172–181. DOI: 10.1007/s13139-019-00588-9.

[14] Robert J. Wilson. "Collimator Technology and Advancements". In: *Journal of Nuclear Medicine Technology* 16.4 (1988).

[15] Hal O. Anger. "Scintillation Camera with Multichannel Collimators". In: *Journal Of Nuclear Medicine* 5 (1964), pp. 515–531.

[16] MICHAEL A. KING et al. "CHAPTER 22 - Attenuation, Scatter, and Spatial Resolution Compensation in SPECT". In: *Emission Tomography*. Ed. by Miles N. Wernick and John N. Aarsvold. San Diego: Academic Press, 2004, pp. 473–498. ISBN: 978-0-12-744482-6. DOI: https://doi.org/10.1016/B978-012744482-6.50025-9. URL: https://www.sciencedirect.com/science/article/pii/B9780127444826500259.

[17] André A. Dobbeleir, Anne-Sophie E. Hambÿe, and Philippe R. Franken. "Influence of high-energy photons on the spectrum of iodine-123 with low- and medium-energy collimators: Consequences for imaging with 123 I-labelled compounds in clinical practice". In: *European Journal of Nuclear Medicine and Molecular Imaging* 26.6 (1999), pp. 655–658. DOI: 10.1007/s002590050434.

[18] H O Anger. "USE OF A GAMMA RAY PINHOLE CAMERA FOR IN-VIVO STUDIES". In: (Feb. 1952). URL: https://www.osti.gov/biblio/4391662.

[19] Z.H. Cho. "Tomography". In: *Encyclopedia of Physical Science and Technology (Third Edition)*. Ed. by Robert A. Meyers. Third Edition. New York: Academic Press, 2003, pp. 843–877. ISBN: 978-0-12-227410-7. DOI: https://doi.org/10.1016/B0-12-227410-5/00965-0. URL: https://www.sciencedirect.com/science/article/pii/B0122274105009650.

[20] Todd E Peterson and Lars R Furenlid. "SPECT detectors: The anger camera and beyond". In: *Physics in Medicine and Biology* 56.17 (2011). DOI: 10.1088/0031-9155/56/17/r01.

[21] J B Svedberg. "On the intrinsic resolution of a gamma camera system". In: *Physics in Medicine and Biology* 17.4 (1972), pp. 514–524. DOI: 10.1088/0031-9155/17/4/005.

[22] GLENN F. KNOLL. *Radiation detection and measurement*. JOHN WILEY, 2020.

[23]   Wilco J Koppert et al. "A comparative study of NaI(Tl), CeBr3, and CZT for use in a real-time simultaneous nuclear and fluoroscopic dual-layer detector". In: *Physics in Medicine amp; Biology* 64.13 (2019), p. 135012. DOI: `10.1088/1361-6560/ab267c`.

[24]   G. L. Miller. *The physics of semiconductor radiation detectors*. Brookhaven National Laboratory, 1961.

[25]   Cédric Desmonts et al. "Evaluation of a new multipurpose whole-body CZT-based camera: Comparison with a dual-head anger camera and first clinical images". In: *EJNMMI Physics* 7.1 (2020). DOI: `10.1186/s40658-020-0284-5`.

[26]   Daniel Roth. "Computational and experimental methods for imaging and dosimetry in 177Lu radionuclide therapy: Classical and novel gamma cameras". English. Defence details Date: 2021-05-28 Time: 09:00 Place: Gamla biskopshuset, Lund. Join via zoom: https://lu-se.zoom.us/j/62859661012?pwd=NVVja2tZd0pndzFuU1hWaEZZRC84dz09 passcode: 2020 External reviewer(s) Name: Erlandsson, Kjell Title: FD Affiliation: Institute of Nuclear Medicine, UCH, 235 Euston Rd, NW1 2BU London, UK —. PhD thesis. Medical Radiation Physics, Lund, 2021. ISBN: 978-91-7895-849-8.

[27]   Jae Cheon Kim et al. "Charge sharing in common-grid pixelated CdZnTe detectors". In: *Nuclear Instruments and Methods in Physics Research Section A: Accelerators, Spectrometers, Detectors and Associated Equipment* 654.1 (2011), pp. 233–243. ISSN: 0168-9002. DOI: `https://doi.org/10.1016/j.nima.2011.06.038`. URL: `https://www.sciencedirect.com/science/article/pii/S0168900211011545`.

[28]   Jen Beatty. "The Radon Transform and the Mathematics of Medical Imaging". PhD thesis. Digital Commons, 2012.

[29]   Miles N. Wernick, John N. Aarsvold, and David S. Lalush. "Iterative Image Reconstruction". In: *Emission tomography: The Fundamentals of Pet and Spect*. Elsevier Academic Press, 2004, pp. 443–472.

[30]   L. A. Shepp and Y. Vardi. "Maximum likelihood reconstruction for emission tomography". In: *Journal of Computer Assisted Tomography* 7.3 (1983), p. 571. DOI: `10.1097/00004728-198306000-00080`.

[31]   H.M. Hudson and R.S. Larkin. "Accelerated image reconstruction using ordered subsets of projection data". In: *IEEE Transactions on Medical Imaging* 13.4 (1994), pp. 601–609. DOI: `10.1109/42.363108`.

[32]   David S Lalush and Benjamin MW Tsui. "Performance of ordered-subset reconstruction algorithms under conditions of extreme attenuation and truncation in myocardial SPECT". In: *Journal of Nuclear Medicine* 41.4 (2000), pp. 737–744.

[33]   Tuija Kangasmaa, Antti Sohlberg, and Jyrki T. Kuikka. "Reduction of collimator correction artefacts with Bayesian reconstruction in Spect". In: *International Journal of Molecular Imaging* 2011 (2011), pp. 1–6. DOI: `10.1155/2011/630813`.

[34]   Kenneth M. Hanson. "Introduction to bayesian image analysis". In: *SPIE Proceedings* (1993). DOI: `10.1117/12.154577`.

[35]   A.R. De Pierro and M.E.B. Yamagishi. "Fast em-like methods for maximum "a posteriori" estimates in emission tomography". In: *IEEE Transactions on Medical Imaging* 20.4 (2001), pp. 280–288. DOI: `10.1109/42.921477`.

[36]   P.J. Green. "Bayesian reconstructions from emission tomography data using a modified EM algorithm". In: *IEEE Transactions on Medical Imaging* 9.1 (1990), pp. 84–93. DOI: `10.1109/42.52985`.

[37]   Tuija S. Kangasmaa, Chris Constable, and Antti O. Sohlberg. "Quantitative Bone Spect/CT reconstruction utilizing anatomical information". In: *EJNMMI Physics* 8.1 (2021). DOI: `10.1186/s40658-020-00348-1`.

[38]   M.A. LODGE. "NUCLEAR MEDICINE IMAGING DEVICES". In: *Nuclear Medicine Physics*. Ed. by E.C.Editor Frey. International Atomic Energy Agency, 2014, pp. 312–397.

[39]   Ronald J. Jaszczak et al. "Improved SPECT Quantification Using Compensation for Scattered Photons". In: *Journal of Nuclear Medicine* 25.8 (1984), pp. 893–900. ISSN: 0161-5505. eprint: `https://jnm.snmjournals.org/content/25/8/893.full.pdf`. URL: `https://jnm.snmjournals.org/content/25/8/893`.

[40]   T OGAWA. "Accurate scatter correction in single photon emission CT". In: *Ann. Nucl. Med. Sci.* 7 (1994), pp. 145–150.

[41]   Zemei Liu, P. Hendrik Pretorius, and Michael Ljungberg. "Simple Monte Carlo based scatter compensation for SPECT". In: *Journal of Nuclear Medicine* 51.supplement 2 (2010), pp. 1354–1354. ISSN: 0161-5505. eprint: `https://jnm.snmjournals.org/content`. URL: `https://jnm.snmjournals.org/content/51/supplement_2/1354`.

[42]   Habib Zaidi, E. C. Frey, and B. M. W. Tsui. "Collimator-Detector Response Compensation in SPECT". In: *Quantitative analysis in nuclear medicine imaging*. Springer, 2006, pp. 141–164.

[43]   Laetitia Imbert et al. "360° CZT gamma cameras for Nuclear Medicine and Molecular Imaging". In: *Nuclear Medicine and Molecular Imaging* (2022), pp. 390–399. DOI: `10.1016/b978-0-12-822960-6.00087-9`.

[44]   Valentina Ferri, Rani Zananiri, and Andrei Iagaru. "Performance evaluation of a novel multi-detector CZT-based SPECT/CT system using Tc99m and Lu177". In: *Journal of Nuclear Medicine* 63.supplement 2 (2022), pp. 2440–2440. ISSN: 0161-5505. eprint: `https://jnm.snmjournals.org/content`. URL: `https://jnm.snmjournals.org/content/63/supplement_2/2440`.

[45]   Yoonsuk Huh et al. "Simulation studies of a full-ring, CZT SPECT system for whole-body imaging of 99mTc and 177Lu". In: *Medical Physics* (2023). DOI: `10.1002/mp.16360`.

[46]   Hong Song et al. "SPECT at the speed of PET: A feasibility study of CZT-based whole-body SPECT/CT in the post 177LU-dotatate and 177LU-PSMA617 setting". In: *European Journal of Nuclear Medicine and Molecular Imaging* (2023). DOI: `10.1007/s00259-023-06176-6`.

[47]   Atharva Aalok. *Professional Plots*. MATLAB Central File Exchange. Retrieved April, 2023. 2023. URL: `https://www.mathworks.com/matlabcentral/fileexchange/100766-professional-plots`.

[48]   Toshimune Ito et al. "Experimental evaluation of the GE NM/CT 870 CZT clinical SPECT system equipped with Wehr and MEHRS Collimator". In: *Journal of Applied Clinical Medical Physics* 22.2 (2021), pp. 165–177. DOI: `10.1002/acm2.13158`.

[49]   *Flanged Jaszczak ECT Phantoms*. 2020. URL: `https://www.spect.com/wp-content/uploads/2020/04/Flanged-Jaszczak-Phantoms.pdf`.

[50]   DataSpectrum. *NEMA IEC PET Body Phantom (NU 2-2018)™*. 2020. URL: `https://www.gammadata.se/assets/Uploads/NEMA-IEC-PET-Body-Phantom.pdf`.

[51]   *Hollow Sphere – 60 mm™, Model ECT/HS-60/A*. 2021. URL: `https://www.spect.com/wp-content/uploads/2021/05/Hollow-Sphere-and-Shells.pdf`.

[52]   *Hollow Sphere Set 6™, Model ECT/HS/SET6*. 2021. URL: `https://www.spect.com/wp-content/uploads/2021/05/Hollow-Sphere-Set-6.pdf`.

[53]   M Holstensson et al. "Model-based correction for scatter and tailing effects in simultaneous99mtc and123I imaging for a CdZnTe cardiac SPECT camera". In: *Physics in Medicine and Biology* 60.8 (2015), pp. 3045–3063. DOI: `10.1088/0031-9155/60/8/3045`.

[54]   Agnetha Gustafsson et al. "Dual-window scatter correction and energy window setting in cerebral blood flow SPECT: A Monte Carlo Study". In: *Physics in Medicine and Biology* 45.11 (2000), pp. 3431–3440. DOI: `10.1088/0031-9155/45/11/323`.

[55]   John C. Dickson et al. "EANM practice guideline for quantitative SPECT-CT". In: *European Journal of Nuclear Medicine and Molecular Imaging* 50.4 (2022), pp. 980–995. DOI: `10.1007/s00259-022-06028-9`.

[56]   Jean-Mathieu Beauregard et al. "Quantitative 177 lu spect (QSPECT) imaging using a commercially available SPECT/CT System". In: *Cancer Imaging* 11.1 (2011), pp. 56–66. DOI: `10.1102/1470-7330.2011.0012`.

[57]   Anna Sundlöv et al. "Individualised 177lu-dotatate treatment of neuroendocrine tumours based on kidney dosimetry". In: *European Journal of Nuclear Medicine and Molecular Imaging* 44.9 (2017), pp. 1480–1489. DOI: `10.1007/s00259-017-3678-4`.

[58]   Atsuro Suzuki et al. "Monte Carlo-based scatter correction considering the tailing effect of a CdTe detector for dual-isotope brain SPECT imaging". In: *Biomedical Physics Engineering Express* 2.4 (July 2016), p. 045010. DOI: `10.1088/2057-1976/2/4/045010`. URL: `https://dx.doi.org/10.1088/2057-1976/2/4/045010`.

[59]   Steve D. Mann and Martin P. Tornai. "Initial evaluation of a modified dual-energy window scatter correction method for CZT-based gamma cameras for breast SPECT". In: *Medical Imaging 2015: Image Processing*. Ed. by Sébastien Ourselin and Martin A. Styner. Vol. 9413. International Society for Optics and Photonics. SPIE, 2015, p. 94132X. DOI: `10.1117/12.2082195`. URL: `https://doi.org/10.1117/12.2082195`.

[60]   Alain Seret. "Median root prior and ordered subsets in Bayesian image reconstruction of single-photon emission tomography". In: *European Journal of Nuclear Medicine and Molecular Imaging* 25.3 (1998), pp. 215–219. DOI: `10.1007/s002590050219`.